Article

Permafrost slows Arctic riverbank erosion

https://doi.org/10.1038/s41586-024-07978-w

Received: 6 March 2024

Accepted: 21 August 2024

Published online: 9 October 2024

Check for updates

Emily C. Geyman[1]✉, Madison M. Douglas[1,2], Jean-Philippe Avouac[1] & Michael P. Lamb[1]

The rate of river migration affects the stability of Arctic infrastructure and communities[1,2] and regulates the fluxes of carbon[3,4], nutrients[5] and sediment[6,7] to the oceans. However, predicting how the pace of river migration will change in a warming Arctic[8] has so far been stymied by conflicting observations about whether permafrost[9] primarily acts to slow[10,11] or accelerate[12,13] river migration. Here we develop new computational methods that enable the detection of riverbank erosion at length scales 5–10 times smaller than the pixel size in satellite imagery, an innovation that unlocks the ability to quantify erosion at the sub-monthly timescales when rivers undergo their largest variations in water temperature and flow. We use these high-frequency observations to constrain the extent to which erosion is limited by the thermal condition of melting the pore ice that cements bank sediment[14], a requirement that will disappear when permafrost thaws, versus the mechanical condition of having sufficient flow to transport the sediment comprising the riverbanks, a condition experienced by all rivers[15]. Analysis of high-resolution data from the Koyukuk River, Alaska, shows that the presence of permafrost reduces erosion rates by 47%. Using our observations, we calibrate and validate a numerical model that can be applied to diverse Arctic rivers. The model predicts that full permafrost thaw may lead to a 30–100% increase in the migration rates of Arctic rivers.

Does permafrost—defined as ground that remains below 0 °C for at least two consecutive years[9]—act primarily to slow[10,11] or accelerate[12,13] the rate of riverbank erosion? This still-unanswered question is fundamental to understanding how the geochemical fluxes[3,16], water quality[17], ecology[5] and infrastructure[1,18] in Arctic watersheds will respond to the approximately 4 °C rising Arctic air temperatures[8] and roughly 40% decrease in permafrost[19] predicted in the coming century[9,19]. Observations of river migration from remotely sensed imagery[10,12,20] have been used to reach opposite conclusions about the role of permafrost in regulating the pace of riverbank erosion. For example, one recent study[10] found that erosion rates in rivers flowing through permafrost are about nine times slower than those in non-permafrost terrains. By contrast, another study[12] found that, for channels of the same width, permafrost rivers migrate faster than their non-permafrost counterparts. This apparent discordance highlights the limitations of regional or global comparisons[10,12], as differences in migration rates from river to river can be caused by myriad confounding variables, including flow seasonality[21], river-ice break-up intensity[21], bank-material cohesion[22] and riverine sediment load[23], rather than the presence or absence of permafrost.

Here we show how analysis of an individual river lets us control for many of these confounding variables and use natural variations in water temperature, discharge and bank-material properties to isolate the thermal and mechanical controls on bank erosion. Specifically, we use variations in water temperature and discharge that occur over timescales of weeks (not years or decades as used in previous work[10,12,20,24]), because the changes in flow conditions that Arctic rivers experience on these sub-seasonal timescales exceed the decadal-scale variability by more than an order of magnitude[25]. However, observing bank erosion at such high frequencies was previously not possible because it requires detecting changes that are much smaller than the pixel size of satellite imagery. We develop computational tools to resolve riverbank erosion at length scales roughly 100 times finer than previous analyses[20] (owing to a ten-times improvement in detection from our new algorithm and a ten-times improvement in the resolution of widely available satellite imagery). We then apply our methodology to the Koyukuk River in central Alaska (Fig. 1a,b), a river that both (1) experiences strong seasonality in water temperature and discharge and (2) flows through discontinuous permafrost, making it particularly well suited to address whether and how permafrost affects river migration.

Using space and time to constrain the role of permafrost

We introduce three sets of observations to test the hypothesis that permafrost limits the pace of river migration.

The spatial pattern of bank erosion

Rivers flowing through discontinuous permafrost offer exceptional natural experiments because a single river (with a given hydrograph, seasonal pattern of water temperature and downstream sediment flux) encounters riverbanks that are variably frozen versus unfrozen. Thus, measurements of local bank erosion rates in permafrost versus non-permafrost terrains in the same river allow us to control for many confounding variables and isolate the role of bank thermal properties on erosion.

[1]Division of Geological and Planetary Sciences, California Institute of Technology, Pasadena, CA, USA. [2]Department of Earth, Atmospheric, and Planetary Sciences, Massachusetts Institute of Technology, Cambridge, MA, USA. ✉e-mail: egeyman@caltech.edu

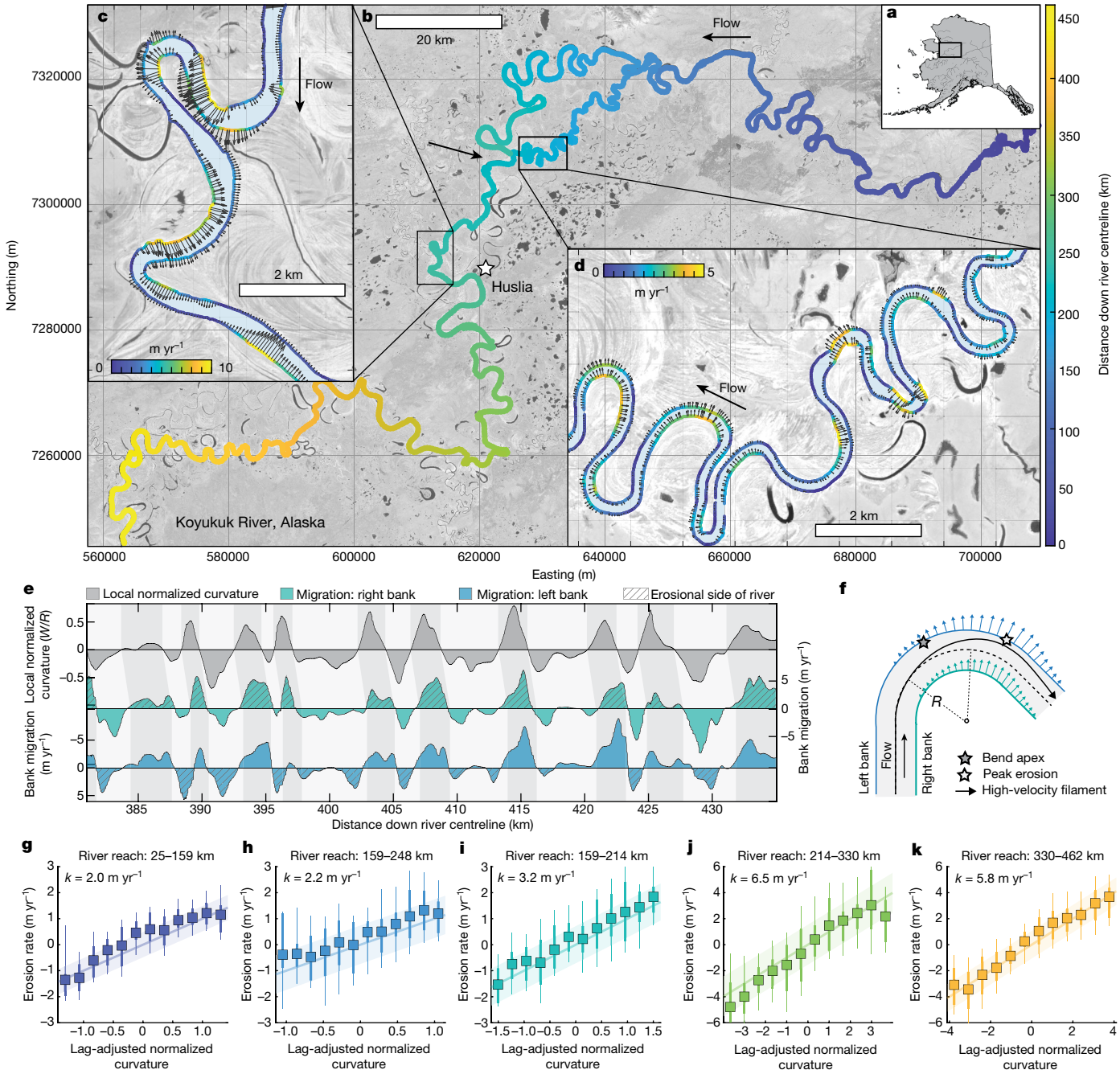

Fig. 1 | Riverbank migration rates quantified for the approximately 450-km-long alluvial reach of the Koyukuk River near Huslia, Alaska. **a**, Map of the study area in Alaska. **b**–**d**, The bank migration rates are calculated by applying our sub-pixel algorithm to a pair of Sentinel-2 satellite images from 30 August 2016 and 13 July 2022. Coordinates are in UTM zone 4N. **c**,**d**, Zoomed-in maps of the bank displacement illustrating how there is a strong relationship between the migration rates and channel curvature[24,39]. **e**, The three spatial series—(1) normalized channel curvature (channel width W divided by radius of curvature R)[24,39], (2) migration of the right bank, and (3) migration of the left bank—all are measured independently. The similarity of the three curves highlights the strong control of channel curvature on migration rate[24]. Note that the channel migration lags the curvature by a distance of about 700 m, or approximately 2.2 channel widths. **f**, Cartoon, adapted from ref. 40, illustrating the source of the lag; as the river moves around a bend, the high-velocity core of the flow impinges on the outer bank at a distance downstream from the bend apex[24,39,40]. **g**–**k**, The local outer-bank erosion rate (see **e**)is explained well by the lag-adjusted normalized curvature (equation (26)). k denotes the curvature-normalized riverbank erosion rate. The colour scheme in **g**–**k** matches the locations in **b**.

The sub-seasonal pattern of bank erosion

The widespread conceptual model for why permafrost may limit the pace of bank erosion is that pore ice strengthens bank sediments to the point that, in order to be eroded by flowing water, those sediments must first be thawed[10,14,26,27]. Thus, the bottleneck of heat transfer from the river water to the frozen bank sediments[27] imposes a speed limit on bank erosion that is not experienced by low-latitude rivers[14]. However, the observation that permafrost riverbanks often have an approximately 1-m-thick layer of thawed sediment at their surface in late summer[10,28] suggests that permafrost rivers are also limited by the ability of flowing river water to entrain and transport sediment[14]. Douglas et al.[14] thus proposed a simple theoretical framework in which bank erosion in permafrost rivers is limited by the joint constraints

of thaw and entrainment. Because Arctic river water tends to be very cold (for example, ≤2 °C) during the period of peak streamflow in early spring (Extended Data Fig. 1), early-season erosion is limited by the ability of the water to thaw the bank material. Then, as the water warms, the river more rapidly transports heat into the bank. However, the discharge is no longer high enough to entrain thawed bank sediment[14]. This model suggests that peak erosion occurs in the early summer at the intersection of still relatively high discharge but warmer waters. By contrast, if permafrost rivers are purely entrainment-limited, the seasonal pattern of erosion only should track discharge, and if permafrost rivers are purely thaw-limited, the seasonal pattern of erosion predominantly should track water temperature[14]. Finally, if bank erosion in Arctic rivers is dominated by ice-run gouging[21], erosive activity should occur primarily during the few-days period of ice break-up[21]. To summarize, the different proposed mechanisms produce distinctive temporal (sub-seasonal) fingerprints of bank erosion (Extended Data Fig. 1).

The interannual pattern of bank erosion

The hydrographs of Arctic rivers vary substantially from year to year. Some years have substantial August rains, leading to high discharge during a period when the river water is warm. Alternatively, in some years, the flow required for sediment entrainment only occurs during the period of spring snowmelt, when the river water is very cold (Extended Data Figs. 1–3). This interannual variability means that total annual erosion may vary by a factor of about three from year to year (Extended Data Fig. 4). Notably, the thaw-limited, entrainment-limited and combined models predict different fingerprints for which years have more or less erosion, meaning that we also can use interannual erosion patterns to distinguish between mechanisms.

Resolving change at sub-pixel length scales

The three sets of observations described above provide independent, data-driven ways to test whether and how permafrost affects the rate of riverbank erosion. Given the remote location of Arctic rivers and the need to make observations across large spatial and temporal scales, quantifying river migration from remotely sensed imagery is a natural choice. However, average migration rates of even the largest Arctic rivers are on the order of 10^0 m yr^{-1} (refs. 10,20), meaning that observational windows of about 3–30 years are required to observe one pixel's worth of change in satellite imagery. Previous methods for quantifying river migration rates use whole-pixel classification[10,20,24,29]. Here we develop a new method that enables detection of river migration at scales 5–10 times smaller than the pixel width. This method allows for the quantification of bank erosion over shorter timescales. For example, consider a large Arctic river migrating at a rate of 3 m yr^{-1} (refs. 10,12,30). Existing methods (which involve the whole-pixel binary masking of 30-m Landsat satellite imagery[20,29]) might require time intervals of about 10 years to robustly detect erosion. By contrast, our new method, when paired with PlanetScope imagery (3-m resolution), can detect movements in the riverbank of about 0.3–0.6 m, meaning that we can subdivide the 3 m yr^{-1} average erosion rates into 5–10 discrete intervals each year and thereby resolve the sub-seasonal pattern of erosion to test the second and third hypotheses above.

Fourier methods for change detection

Our algorithm for detecting bank migration is based on sub-pixel correlation of optical satellite imagery[31] (Fig. 1). Consider an image of a river and surrounding floodplain (Fig. 1b). Let the outer bank of the river erode a distance equivalent to one-tenth the pixel width. Such a change may not be visible by eye but it is recorded in the image data because the pixel intensity values along the river margins will change to reflect the new ratio of water versus floodplain encapsulated in that pixel (Extended Data Fig. 6). One way to quantify this sub-pixel displacement would be to: (1) sample a small $n \times n$-pixel window ('chip') from each image at a location of interest; (2) linearly upsample each image chip by a factor of ten; and then (3) compute the 2D cross-correlation between the two upsampled chips. If the primary source of contrast in the image is the river–floodplain boundary, then the peak in the 2D cross-correlation spectrum will record the riverbank displacement (Extended Data Fig. 6). However, the computational cost of 2D cross-correlation is $\mathcal{O}(n^4)$, where n is the width of the chip. Thus, performing the 2D cross-correlation for every position along the river (Fig. 1) is computationally expensive and difficult to scale to larger rivers, longer time series, or higher-resolution imagery. Thus, we make use of the convolution theorem (that is, the fact that convolution in the spatial domain is equivalent to multiplication in the Fourier domain)[31]. By taking the 2D Fourier transforms of the image chips, taking the complex conjugate of the second image, multiplying the result and then calculating the inverse Fourier transform, we can efficiently detect riverbank erosion at sub-pixel length scales not visible to the human eye. See Methods for a complete description of the algorithm, including data pre-processing routines and sensitivity tests. A critical component of our methodology is a workflow to make the displacement estimates robust to georeferencing errors in the satellite imagery, since image-to-image co-registration errors can exceed the signal of riverbank erosion by ≥10 times .

Three tests of whether permafrost slows river migration

Here we show how our observations of the spatial, sub-seasonal, and interannual patterns of riverbank erosion on the Koyukuk River (Fig. 1) all independently demonstrate that permafrost slows the pace of river migration.

The spatial pattern of bank erosion

As shown previously for low-latitude rivers[24], river curvature represents the dominant control on migration rates (Fig. 1e); tight bends migrate at rates >5 m yr^{-1}, whereas the straight reaches between them experience erosion rates ≥10 times lower (Fig. 1c,d). Most previous analyses have not corrected migration rates for the effects of curvature[10,12]. Here we quantify the first-order relationship between river curvature and migration rate (Fig. 1g–k) and then examine the deviations from this trend. Specifically, we take advantage of the fact that the Koyukuk River flows through discontinuous permafrost[10,16,32]. As the river flows against heterogeneous bank material[16], we can ask whether there is a systematic difference in the curvature-normalized erosion rates for permafrost versus non-permafrost terrain. For example, Fig. 2a–c shows an example of a sequence of meander bends that impinge on older, thermokarst terrain to the north and younger, unfrozen river deposits to the south. We calculate the river curvature and the bank migration rate for each meander bend over a 6-year period (Fig. 2d). The ratio of the area under the curve for these two variables (Fig. 2) records the average k value for each meander, in which k is the curvature-normalized migration rate (m yr^{-1}). Qualitatively, larger values of k imply that the riverbank is more susceptible to erosion. In Fig. 2e–g, we search along the entire 450-km reach of the Koyukuk River shown in Fig. 1b and investigate whether meanders through high-permafrost terrains have systematically higher or lower erosion rates. Meanders traversing terrains classified as non-permafrost (Extended Data Fig. 10) migrate 91% faster for a given river curvature than those migrating through permafrost terrains (Fig. 2e).

Note that, when considered in isolation, the results in Fig. 2 present us with a 'chicken or the egg' problem. The fact that non-permafrost reaches experience channel migration rates about two times faster than permafrost reaches could imply that permafrost banks slow the pace of riverbank erosion. However, given the slow rate of permafrost regeneration (about 10^3 years, as constrained by ^{14}C dating

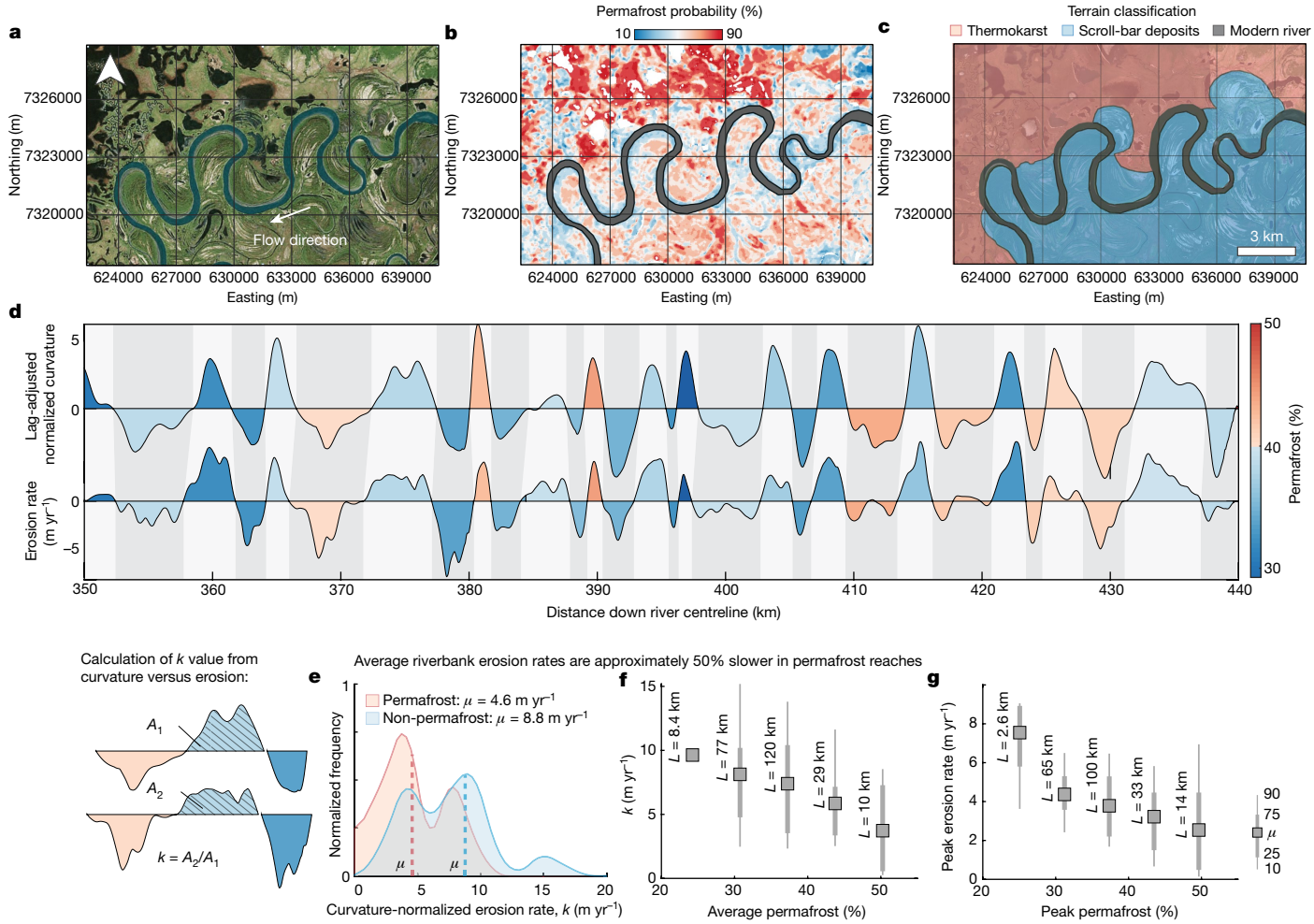

Fig. 2 | Spatial observations show that riverbank erosion rates are systematically slower in meanders that erode permafrost compared with those that erode unfrozen terrain. a, RGB satellite imagery. **b**, Probability of near-surface permafrost[32]. **c**, Simplified terrain classification for a series of meander bends on the Koyukuk River (Fig. 1). Note how the river impinges on older, thermokarst terrain to the north and younger, non-permafrost terrain to the south. **d**, Spatial series of lag-adjusted normalized curvature (see equation (26))[24,39] and riverbank erosion rates. The crossovers reflect the places at which the river transitions from eroding its right bank to eroding its left bank, or vice versa. The colour of the shaded infill reflects the mean permafrost probability[32] calculated for the eroding side of the meander. For each meander, dividing the riverbank erosion rate (A_2) by the lag-adjusted normalized curvature (A_1) yields a bend-averaged value of k, the curvature-normalized erosion rate (m yr^{-1}) (see equation (27)). **e**, Bends classified as permafrost[32,33] (Extended Data Fig. 10) have mean k values of 4.6 m yr^{-1}, whereas bends classified as non-permafrost have mean k values of 8.8 m yr^{-1}. **f**,**g**, The k values systematically decrease with increasing average (**f**) and maximum (**g**) permafrost content[32] calculated over the meander bend. In **f** and **g**, the L annotations signify the length of the river reaches that fall within each bin for average and peak permafrost content. The satellite imagery in **a** is from Bing Maps Aerial, reprinted with permission from Microsoft Corporation.

along the Koyukuk River[33]), river reaches that are migrating rapidly across their floodplain will be eroding into alluvial material that is younger[4] and therefore more likely to be unfrozen. Thus, the arrow of causation could be drawn in the opposite direction, in which rapid channel migration—owing to non-thermal controls such as elevated sediment supply[23] at the relic Pleistocene aeolian sand dunes near Huslia (Fig. 1a) or increases in river slope in response to meander cut-offs[34]—could cause local riverbanks to have lower permafrost content. To explicitly test whether there is a thermal control on erosion rates, we turn to the temporal pattern of riverbank erosion.

The sub-seasonal pattern of bank erosion

The variations in river temperature and discharge within a single spring season on the Koyukuk River (Extended Data Fig. 1) are more than an order of magnitude larger than the long-term, decadal trends in those variables[25]. Following ice break-up in May, the water discharge spikes. During this period of high snowmelt, the water temperature is close to 0 °C. The water temperature peaks around 17 °C in mid-July, when the water discharge is low (Extended Data Fig. 1). Here we follow Douglas et al.[14] and consider simple, semi-empirical predictions for the seasonal pattern of riverbank erosion under the competing endmembers that: (1) erosion is limited by the ability of warm river water to thaw the pore ice in bank sediments[26,27,35] or (2) erosion is limited by the ability of the river to entrain the sediment comprising the river bed and banks[15,36,37]. In the thaw-limited endmember, the erosion rate is described by the function[27,35]:

$$E_{\mathrm{thaw}} = \frac{A\mathrm{Pr}^{\alpha}\mathrm{Re}^{\beta}\kappa_{\mathrm{w}}T_{\mathrm{w}}}{H\rho_{\mathrm{b}}\left(L_{\mathrm{f}} - c_{\mathrm{p}}T_{\mathrm{i}}\right)} \quad (1)$$

in which Pr is the Prandtl number, Re is the Reynolds number, κ_{w} (W m^{-1} °C^{-1}) is the thermal conductivity of water, T_{w} (°C) is the water temperature, T_{i} (°C) is the initial temperature of permafrost, L_{f} (J kg^{-1}) is the latent heat of fusion for permafrost, ρ_{b} (kg m^{-3}) is the bulk density of permafrost and c_{p} (J kg^{-1} °C^{-1}) is the heat capacity of permafrost.

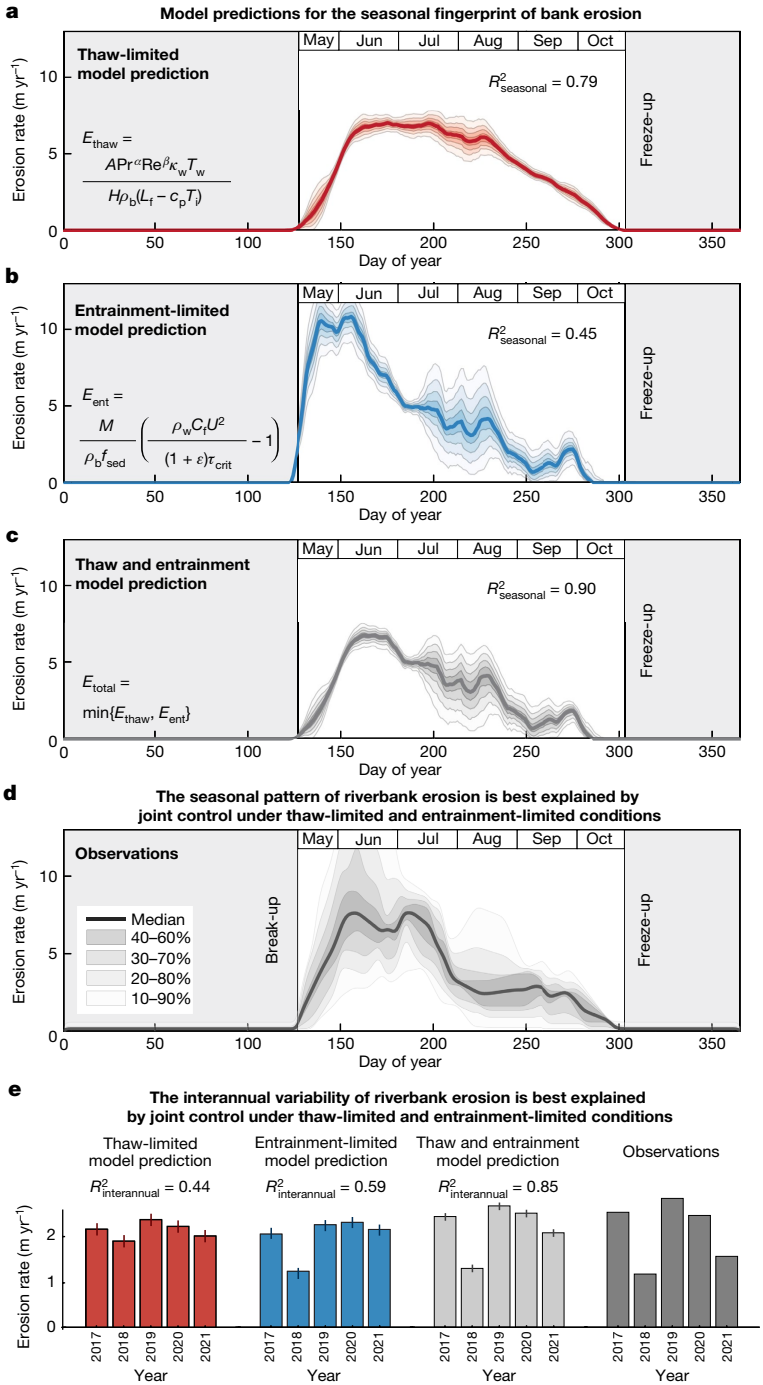

Fig. 3 | Model predictions for—and observations of—the temporal patterns of riverbank erosion. a–**c**, The water temperature and discharge time series for the Koyukuk River (Extended Data Figs. 1–3) are combined with equations (1) and (2) to make predictions for the erosion rate throughout the annual cycle under the thaw-limited (**a**), entrainment-limited (**b**) and combined (**c**) regimes. **d**, The observed annual pattern of erosion rates (based on data from 2016 to 2022) best matches the predictions from the combined thaw-limited and entrainment-limited model. The R^2 values in **a**–**c** give the goodness of fit of the model predictions to the observations in **d**. Note that we only study the seasonal pattern of bank displacement on the eroding side of the river. The time series from the accreting side of the river should record seasonal patterns of vegetation colonization and sediment deposition. See Section 2 of the Supplementary Information. **e**, Model predictions for and observations of the interannual pattern of bank erosion. The error bars represent uncertainty in the model parameters based on leave-one-out cross-validation (iteratively solving for the optimal model parameters using 4 of the 5 years in the dataset). The observed interannual pattern is best explained by the combined thaw and entrainment model (R^2 = 0.85).

In equation (1), the numerator represents the heat transfer rate from the river water to the bank and the denominator represents the heat required to thaw the bank[14,27].

In the entrainment-limited endmember, the erosion rate can be calculated using the common threshold formulation[38], adapted to mixtures of sediment and ice[14]:

$$E_{ent} = \frac{M}{\rho_b f_{sed}}\left(\frac{\rho_w C_f U^2}{(1+\epsilon)\tau_{crit}} - 1\right) \quad (2)$$

in which τ_{crit} (Pa) is the critical shear stress required to entrain sediment, $f_{sed} = 1 - f_{ice}$ (dimensionless) is the mass fraction of sediment,

ρ_w (kg m^{-3}) is the density of water, U (m s^{-1}) is the average flow velocity, C_f is the dimensionless friction coefficient, $\epsilon \approx 0.2$ is a small coefficient in the 'near-threshold' model[15,36,37] and M (kg m^{-2} s^{-1}) is an empirical coefficient describing the erodibility of the bank[14,38]. See Methods for a discussion of the assumptions underpinning equations (1) and (2).

The thaw-limited endmember (equation (1)) predicts that erosion scales like the product of the flow velocity and the water temperature. Meanwhile, the entrainment-limited endmember (equation (2)) predicts that the erosion rate scales with the flow velocity squared (see Methods). By applying these two sets of predictions to the water temperature and discharge time series for the Koyukuk River over the period 2016–2022 (Extended Data Figs. 1–3), we generate model predictions for the seasonal pattern of riverbank erosion (Fig. 3a,b). The joint constraint that the river must be able to both thaw frozen bank material and entrain the thawed sediment is represented by the minimum of the thaw-limited and entrainment-limited rates[14] (Fig. 3c). Next we compile 61 cloud-free daily image mosaics of PlanetScope satellite imagery over the period 2016–2022. We use our sub-pixel riverbank change detection algorithm to quantify erosion at every location along the 450-km river reach shown in Fig. 1b. The observed sub-seasonal pattern of erosion (Fig. 3d) matches the predictions from the combined thaw-limited and entrainment-limited model ($R^2 = 0.90$) better than the thaw-only ($R^2 = 0.79$) or entrainment-only ($R^2 = 0.45$) models.

Interannual variability of bank erosion

The natural year-to-year variability in discharge and temperature means that interannual observations can also constrain what processes control erosion. The thaw-limited model predicts that all years in our study window should have relatively equal erosion rates (Fig. 3e). Meanwhile, the entrainment-limited model predicts that 2018 was a year of low erosion (Fig. 3e). Finally, the combined thaw-limited and entrainment-limited model predicts that both 2018 and 2021 stand out as low-erosion years. This combined model best matches the observed interannual pattern of erosion (Fig. 3e; $R^2 = 0.85$), validating our interpretation from the sub-seasonal observations (Fig. 3d) that the migration behaviour of the Koyukuk River is controlled by the joint constraints of thaw and entrainment.

Modelling future erosion behaviour

Our calibration and validation of models describing the spatial[24,39] (Fig. 1b) and temporal (Fig. 3) patterns of riverbank erosion enables us to run numerical simulations to predict how Arctic rivers may respond to the forecasted increases in water temperature[8], discharge seasonality[8,18] and permafrost thaw[9,19]. In Extended Data Fig. 5, we perform a series of numerical experiments in which we perturb the water temperature and discharge. We find that riverbank erosion is relatively insensitive to increases in water temperature on the Koyukuk River, as the system quickly becomes entrainment-limited (Extended Data Fig. 1). For example, if the total discharge (Q_w) remains constant, increases in water temperature of 10% and 30% only result in increases in bank erosion of 4% and 9%, respectively. However, bank erosion scales approximately linearly with the total discharge; increases in Q_w of 10% and 30% elevate bank erosion by 12% and 34%, respectively. Finally, under the scenario of complete permafrost thaw[9,19], increases in Q_w of 10% and 30% result in increases of average bank erosion of 69% and 109%, respectively (Extended Data Fig. 5).

Implications for a changing Arctic

Riverbank erosion jeopardizes the stability of Arctic infrastructure and communities[1,18], especially in Alaska, where 43% of villages are located ≤1 km from rivers[10]. The rate of river migration also sets the cadence of organic carbon cycling between floodplains, river water, the atmosphere and the ocean[4,16]. Because bank erosion can liberate carbon from depths ≥10 times the depth of annual thaw[16], river migration may prove to be one of the most efficient mechanisms for organic carbon turnover in the Arctic[3]. In other words, the pace of river migration may represent a critical bottleneck affecting the timescale over which the 1,700 billion metric tons of carbon locked up in Arctic permafrost enters Earth's atmosphere[3,4]. Our observations of the spatial and temporal patterns of riverbank erosion demonstrate that, on the Koyukuk River, the presence of discontinuous permafrost reduces average migration rates by approximately 49% at present. Finally, our numerical model (Fig. 3c) provides a tool to use variables such as the water temperature, river hydraulics and sediment grain size to predict how the rates of riverbank erosion and associated sediment and carbon fluxes will increase as permafrost thaws in the coming centuries[8,9,19].

Online content

Any methods, additional references, Nature Portfolio reporting summaries, source data, extended data, supplementary information, acknowledgements, peer review information; details of author contributions and competing interests; and statements of data and code availability are available at https://doi.org/10.1038/s41586-024-07978-w.

1. Hjort, J. et al. Degrading permafrost puts Arctic infrastructure at risk by mid-century. *Nat. Commun.* **9**, 5147 (2018).
2. Rowland, J. et al. Arctic landscapes in transition: responses to thawing permafrost. *Eos* **91**, 229–230 (2010).
3. Miner, K. R. et al. Permafrost carbon emissions in a changing Arctic. *Nat. Rev. Earth Environ.* **3**, 55–67 (2022).
4. Torres, M. A. et al. Model predictions of long-lived storage of organic carbon in river deposits. *Earth Surf. Dyn.* **5**, 711–730 (2017).
5. Terhaar, J., Lauerwald, R., Regnier, P., Gruber, N. & Bopp, L. Around one third of current Arctic Ocean primary production sustained by rivers and coastal erosion. *Nat. Commun.* **12**, 169 (2021).
6. Zhang, T. et al. Warming-driven erosion and sediment transport in cold regions. *Nat. Rev. Earth Environ.* **3**, 832–851 (2022).
7. Syvitski, J. et al. Earth's sediment cycle during the Anthropocene. *Nat. Rev. Earth Environ.* **3**, 179–196 (2022).
8. Post, E. et al. The polar regions in a 2°C warmer world. *Sci. Adv.* **5**, eaaw9883 (2019).
9. Smith, S. L., O'Neill, H. B., Isaksen, K., Noetzli, J. & Romanovsky, V. E. The changing thermal state of permafrost. *Nat. Rev. Earth Environ.* **3**, 10–23 (2022).
10. Rowland, J. C. et al. Scale-dependent influence of permafrost on riverbank erosion rates. *J. Geophys. Res. Earth Surf.* **128**, e2023JF007101 (2023).
11. Piliouras, A., Lauzon, R. & Rowland, J. C. Unraveling the combined effects of ice and permafrost on Arctic delta morphodynamics. *J. Geophys. Res. Earth Surf.* **126**, e2020JF005706 (2021).
12. Ielpi, A., Lapôtre, M. G., Finotello, A. & Roy-Léveillée, P. Large sinuous rivers are slowing down in a warming Arctic. *Nat. Clim. Change* **13**, 375–381 (2023).
13. Kanevskiy, M. et al. Patterns and rates of riverbank erosion involving ice-rich permafrost (yedoma) in northern Alaska. *Geomorphology* **253**, 370–384 (2016).
14. Douglas, M. M., Dunne, K. B. & Lamb, M. P. Sediment entrainment and slump blocks limit permafrost riverbank erosion. *Geophys. Res. Lett.* **50**, e2023GL102974 (2023).
15. Phillips, C. B. et al. Threshold constraints on the size, shape and stability of alluvial rivers. *Nat. Rev. Earth Environ.* **3**, 406–419 (2022).
16. Douglas, M. M. et al. Organic carbon burial by river meandering partially offsets bank erosion carbon fluxes in a discontinuous permafrost floodplain. *Earth Surf. Dyn.* **10**, 421–435 (2022).
17. Striegl, R. G., Dornblaser, M. M., Aiken, G. R., Wickland, K. P. & Raymond, P. A. et al. Carbon export and cycling by the Yukon, Tanana, and Porcupine rivers, Alaska, 2001–2005. *Water Resourc. Res.* **43**, W02411 (2007).
18. Teufel, B. & Sushama, L. Abrupt changes across the Arctic permafrost region endanger northern development. *Nat. Clim. Change* **9**, 858–862 (2019).
19. Chadburn, S. et al. An observation-based constraint on permafrost loss as a function of global warming. *Nat. Clim. Change* **7**, 340–344 (2017).
20. Langhorst, T. & Pavelsky, T. Global observations of riverbank erosion and accretion from Landsat imagery. *J. Geophys. Res. Earth Surf.* **128**, e2022JF006774 (2023).
21. Chassiot, L., Lajeunesse, P. & Bernier, J.-F. Riverbank erosion in cold environments: review and outlook. *Earth-Sci. Rev.* **207**, 103231 (2020).
22. Constantine, C. R., Dunne, T. & Hanson, G. J. Examining the physical meaning of the bank erosion coefficient used in meander migration modeling. *Geomorphology* **106**, 242–252 (2009).
23. Constantine, J. A., Dunne, T., Ahmed, J., Legleiter, C. & Lazarus, E. D. Sediment supply as a driver of river meandering and floodplain evolution in the Amazon Basin. *Nat. Geosci.* **7**, 899–903 (2014).
24. Sylvester, Z., Durkin, P. & Covault, J. A. High curvatures drive river meandering. *Geology* **47**, 263–266 (2019).
25. Feng, D. et al. Recent changes to Arctic river discharge. *Nat. Commun.* **12**, 6917 (2021).

26. Costard, F. et al. Impact of the global warming on the fluvial thermal erosion over the Lena River in Central Siberia. *Geophys. Res. Lett.* **34**, L14501 (2007).
27. Costard, F., Dupeyrat, L., Gautier, E. & Carey-Gailhardis, E. Fluvial thermal erosion investigations along a rapidly eroding river bank: application to the Lena River (central Siberia). *Earth Surf. Process. Landf.* **28**, 1349–1359 (2003).
28. Scott, K. M. Effects of permafrost on stream channel behavior in Arctic Alaska. Professional Paper 1068. United States Geological Survey (1978).
29. Rowland, J. C. et al. A morphology independent methodology for quantifying planview river change and characteristics from remotely sensed imagery. *Remote Sens. Environ.* **184**, 212–228 (2016).
30. Langhorst, T. & Pavelsky, T. M. Global observations of riverbank erosion and accretion from Landsat imagery. *J. Geophys. Res. Earth Surf.* **128**, e2022JF006774 (2023).
31. Leprince, S., Barbot, S., Ayoub, F. & Avouac, J.-P. Automatic and precise orthorectification, coregistration, and subpixel correlation of satellite images, application to ground deformation measurements. *IEEE Trans. Geosci. Remote Sens.* **45**, 1529–1558 (2007).
32. Pastick, N. J. et al. Distribution of near-surface permafrost in Alaska: estimates of present and future conditions. *Remote Sens. Environ.* **168**, 301–315 (2015).
33. Douglas, M. M. et al. Permafrost formation in a meandering river floodplain. *AGU Adv.* **5**, e2024AV001175 (2024).
34. Finnegan, N. J. & Dietrich, W. E. Episodic bedrock strath terrace formation due to meander migration and cutoff. *Geology* **39**, 143–146 (2011).
35. Douglas, M. M., Miller, K. L., Schmeer, M. N. & Lamb, M. P. Ablation-limited erosion rates of permafrost riverbanks. *J. Geophys. Res. Earth Surf.* **128**, e2023JF007098 (2023).
36. Parker, G. Self-formed straight rivers with equilibrium banks and mobile bed. Part 2. The gravel river. *J. Fluid Mech.* **89**, 127–146 (1978).
37. Dunne, K. B. & Jerolmack, D. J. What sets river width? *Sci. Adv.* **6**, eabc1505 (2020).
38. Partheniades, E. Erosion and deposition of cohesive soils. *J. Hydraul. Div.* **91**, 105–139 (1965).
39. Howard, A. D. & Knutson, T. R. Sufficient conditions for river meandering: a simulation approach. *Water Resour. Res.* **20**, 1659–1667 (1984).
40. Furbish, D. J. River-bend curvature and migration: how are they related? *Geology* **16**, 752–755 (1988).

Methods

Model expectations for entrainment-limited and thaw-limited riverbank erosion

Governing equations. As described in the main text, we present a simple 1D model to try to capture the competing thermal versus physical controls on Arctic riverbank erosion. For the thaw-limited endmember, the erosion rate can be expressed by the function[27,35]:

$$E_{\text{thaw}} = \frac{A\text{Pr}^{\alpha}\text{Re}^{\beta}\kappa_{\text{w}}(T_{\text{w}} - T_{\text{f}})}{H\rho_{\text{b}}\left(L_{\text{f}} + c_{\text{p}}(T_{\text{f}} - T_{\text{i}})\right)} \tag{3}$$

in which κ_{w} (W m^{-1} °C^{-1}) is the thermal conductivity of water, T_{w} (°C) is the river water temperature, T_{f} (°C) is the freezing point of water (assumed to be 0 °C in the main text for simplicity), T_{i} (°C) is the initial temperature of permafrost, L_{f} (J kg^{-1}) is the latent heat of fusion for permafrost ($L_{\text{f}} = f_{\text{ice}}L_{\text{ice}}$, where f_{ice} (kg kg^{-1}) is the mass fraction of water ice in permafrost and L_{ice} (J kg^{-1}) is the latent heat of fusion for water ice), ρ_{b} (kg m^{-3}) is the bulk density of permafrost and c_{p} (J kg^{-1} °C^{-1}) is the heat capacity of permafrost. Pr is the Prandtl number:

$$\text{Pr} = \nu/\chi \tag{4}$$

in which ν (m^2 s^{-1}) is the kinematic viscosity and χ (m^2 s^{-1}) is the thermal diffusivity of the river water. Re is the Reynolds number:

$$\text{Re} = HU/\nu \tag{5}$$

in which H (m) is the flow depth and U (m s^{-1}) is the average flow velocity. Note that we define E_{thaw} only for $T_{\text{w}} \geq 0$.

For the entrainment-limited end-member, we use the common threshold formulation[38]:

$$E_{\text{ent}} = \frac{M}{\rho_{\text{b}}f_{\text{sed}}}\left(\frac{\tau_{\text{bank}}}{\tau_{\text{crit}}} - 1\right)^{n} \tag{6}$$

in which τ_{bank} (Pa) is the shear stress on the bank, τ_{crit} (Pa) is the critical shear stress required to entrain bank sediment, $f_{\text{sed}} = 1 - f_{\text{ice}}$ (dimensionless) is the mass fraction of sediment and M (kg m^{-2} s^{-1}) and n (dimensionless) are empirical coefficients[14,38]. To solve for E_{ent}, we use the following set of assumptions. First, we need a method to partition the total fluid shear stress in the channel (τ) between the channel bed and the bank[41]. To the first order, the bed and bank stress partitioning depends on the relative roughness of the two surfaces and the channel width-to-depth ratio[41–44]. For simplicity, we let the shear stress on the bank (τ_{bank}) follow the near-threshold '$(1 + \epsilon)$' model of Parker[15,36]:

$$\tau_{\text{bank}} = \left(\frac{1}{1+\epsilon}\right)\tau_{\text{bed}} \tag{7}$$

in which $\epsilon = 0.2$ (refs. 15,36). The shear stress on the bed can be related to the flow velocity using a canonical flow-resistance equation[15]:

$$\tau_{\text{bed}} = \rho_{\text{w}}C_{\text{f}}U^2 \tag{8}$$

in which ρ_{w} (kg m^{-3}) is the density of water. Equation (8) is based on the relationship between the cross-sectionally averaged flow velocity, U, and the shear velocity, u_*, through a dimensionless friction coefficient, C_{f}:

$$U = \frac{1}{\sqrt{C_{\text{f}}}}u_* \tag{9}$$

in which u_* is defined as:

$$u_* = \sqrt{\tau_{\text{bed}}/\rho_{\text{w}}} \tag{10}$$

Combining equation (6) with equations (7) and (8), we arrive at the expression:

$$E_{\text{ent}} = \frac{M}{\rho_{\text{b}}f_{\text{sed}}}\left(\frac{\rho_{\text{w}}C_{\text{f}}U^2}{(1+\epsilon)\tau_{\text{crit}}} - 1\right)^{n} \tag{11}$$

We define equation (11) only for $E_{\text{ent}} \geq 0$ m yr^{-1}. Empirical studies often use $n \approx 1$ in the Partheniades[38] erosion relation (equation (6))[14]. This approximation reduces equation (11) to equation (2) of the main text. When $n = 1$, the erosion rate, E_{ent}, is a simple quadratic function of the flow velocity, U, above some critical threshold velocity, U_0, at which erosion starts to occur:

$$E_{\text{ent}} \propto (U - U_0)^2 \tag{12}$$

Meanwhile, setting $\beta = 1$ in equation (3) (refs. 14,27) simplifies the Re$^{\beta}$ term in the numerator to HU/ν, such that the predicted erosion rate from thaw is a function of the product of the flow velocity and water temperature:

$$E_{\text{thaw}} \propto UT_{\text{w}} \tag{13}$$

Thus, although there are many parameters in equations (3) and (11), these expressions make simple predictions for how E_{ent} and E_{thaw} evolve as a function of the seasonal discharge and water temperature time series. The entrainment-limited riverbank erosion should scale with flow velocity squared (equation (12)), whereas the thaw-limited erosion should scale with the product of flow velocity and temperature (°C above freezing) (equation (13)). Moreover, because the water temperature varies by about 20 °C over the course of a seasonal cycle, whereas the flow velocity varies by about 2 m s^{-1} (Extended Data Fig. 4), the seasonal pattern of thaw-limited erosion is controlled roughly ten times more by changes in water temperature than by changes in flow velocity.

Note that our simple model assumes that the state of the riverbank is in local equilibrium with the erosion mode (entrainment-limited or thaw-limited). In other words, our model does not include a 'history effect' that could be important in some cases for building up a thawed layer[45]. However, the numerical modelling of ref. 45 suggests that our local equilibrium assumption is a reasonable one most of the time because the thawed layer thickness rapidly adjusts to changes in either thaw rate or entrainment rate (for which we define 'rapid' compared with the temporal forcing from the hydrograph or the seasonal temperature pattern)[45].

Finally, note that, to predict the seasonal cycles of E_{ent} and E_{thaw}, we must translate the discharge records (Extended Data Fig. 2) into estimates of flow velocity. The water discharge Q_{w} (m^3 s^{-1}) is the product of the cross-sectionally averaged flow velocity (U) and cross-sectional area (A):

$$Q_{\text{w}} = UA. \tag{14}$$

We calculate flow velocity from the discharge record using a simple power-law empirical fit of Q_{w} versus U based on field data from the Koyukuk River (Extended Data Fig. 4a).

Observational constraints for discharge and water temperature on the Koyukuk River. Using equations (3) and (11) to make model predictions for the seasonal pattern of riverbank erosion requires continuous time series of water temperature and discharge on the Koyukuk River. The United States Geological Survey (USGS) maintains a streamflow station on the Koyukuk River at Hughes, Alaska (66.04696° N, 154.26097° W), but this station was inactive from 1982 to 2021 (Extended Data Fig. 2), which covers nearly our entire observational window from 2016 to 2022. However, several USGS gauge

stations on the nearby Yukon and Tanana rivers remained active from 2016 to 2022. An investigation of historical periods of overlap between the Hughes station and stations on the Yukon and Tanana rivers (Extended Data Fig. 2) suggests that the discharge records at these nearby stations can be related using simple convolutional/deconvolutional filters. Specifically, we consider the case of the USGS streamflow stations at Hughes (Koyukuk River), Stevens Village (Yukon River) and Pilot Station (Yukon River) (Extended Data Fig. 2k). The Koyukuk River joins the Yukon River about halfway between Stevens Village and Pilot Station, at which it contributes roughly 10–20% of the Yukon's total discharge. Thus, the difference in discharge measured at Pilot Station versus Stevens Village should encode information about the discharge contribution from the Koyukuk River, modulated by convolutional smoothing and other changes to the Yukon hydrograph that occur from upstream to downstream.

Using autoencoders to fill gaps in observational discharge records. We design a flexible model that can learn the relationships between the hydrographs at Hughes, Pilot Station and Stevens Village using historical data (Extended Data Fig. 2k). Specifically, we train a simple neural network for which the input is a 2×365 array containing the daily discharge time series at Pilot Station and Stevens Village (normalized for numerical stability such that the minimum discharge is 0 and the maximum discharge is 1) and the output is a 1×365 array containing the predicted daily discharge time series at Hughes (Extended Data Fig. 2l). Our neural network architecture consists of a simple 2×33 2D convolutional kernel, a batch normalization layer, a fully connected layer and a regression layer. The neural network was implemented in MATLAB R2022a.

Extended Data Fig. 3a–e shows the data used to train the model (5 years in the historical record when the USGS stations at Hughes, Pilot Station and Stevens Village all had uninterrupted discharge data). In the training dataset, the model is validated using leave-one-out cross-validation. For example, in Extended Data Fig. 3a, the model is trained using the historical data from 1978 to 1981 and then used to predict the Hughes discharge time series from 1977. The R^2 value gives the variance reduction of the neural network model compared with the observed discharge time series. The mean R^2 from all years in the historical (training) dataset is 0.82. Extended Data Fig. 3f–j shows the predictions for the discharge on the Koyukuk River during the years 2017–2021, when the Pilot Station and Stevens Village stations were active, but the Hughes station was not.

Predictions for the sub-seasonal and interannual pattern of riverbank erosion. Extended Data Fig. 4 combines the neural-network-predicted discharge time series for the Koyukuk River (Extended Data Fig. 3) with the Pilot Station temperature data (Extended Data Fig. 1b) to estimate the annual patterns of erosion under the thaw-limited, entrainment-limited and combined scenarios. In Extended Data Fig. 4i–k, we optimize the free parameters in equations (3)–(6) such that the predicted annual erosion (2017–2021) best matches the observations from the Koyukuk River (Extended Data Fig. 4l). Extended Data Table 1 shows the values of the parameters obtained from our nonlinear optimization, along with the values of the fixed parameters used for equations (3)–(6) (ref. 14).

Evaluating model goodness of fit. Note in Extended Data Fig. 4 that we compare models with different numbers of tunable parameters: one parameter for the thaw-only model, two for the entrainment-only model and three for the combined thaw and entrainment model. Thus, the increase in the raw R^2 values shown in Extended Data Fig. 4i–k could reflect the added degrees of freedom in the models rather than an improvement in the description of the underlying process. In an attempt to account for the changing model complexity in our evaluation of the model goodness of fit, we compute the adjusted R^2 value, defined as:

$$R^2_{\mathrm{adj}} = 1 - \frac{(1-R^2)(n-1)}{n-p-1} \tag{15}$$

in which n is the number of data points on which the variance reduction (R^2) is evaluated and p is the number of independent variables (parameters). The p in the denominator of equation (15) acts to penalize models with more tunable parameters (that is, give them a lower R^2_{adj} value). Extended Data Fig. 4i–k shows that the R^2_{adj} values for the thaw-only, entrainment-only and combined thaw and entrainment models are 0.25, 0.14 and 0.40, respectively. In other words, the R^2_{adj} metric supports the conclusion that the combined thaw and entrainment model best explains the interannual data.

Detecting bank erosion from sub-pixel image correlation

Background. Our workflow for detecting sub-pixel displacements is inspired by the methodology of Leprince et al.[31,46] but is adapted to handle both the challenges and the opportunities presented by the fact that riverbanks are predominantly linear features rather than 'corner' features. As an illustration of our approach, consider an example high-resolution image of a riverbank on the Koyukuk River (Extended Data Fig. 6). As a simple experiment, we shift the image by 2 pixels in the x direction and 1 pixel in the y direction. We then downsample the image by a factor of 10, so the Δx and Δy offsets are 0.2 and 0.1 pixels, respectively. The question is whether we can detect these sub-pixel offsets from the downsampled image. One approach would be to compute the 2D cross-correlation between image 1 and image 2. The peak of the resulting cross-correlation spectrum (which can be interpolated to sub-pixel positions) records the bank displacement. When the bank geometry is relatively linear (as is typically the case for images that are smaller than the length scale of the channel width—see the section 'Selecting the window size (n)'), the cross-correlation spectrum does not have a well-resolved single peak but rather a ridge of high correlation values (Extended Data Fig. 6). However, the only probable image offsets are the ones in which the riverbank accreted (migrated towards the channel centreline) or eroded (migrated away from the channel centreline). Thus, a good approximation for riverbank change detection is that the offset vector is perpendicular to the bank. Sampling the image cross-correlation matrix along a vector perpendicular to the riverbank yields a peaked function whose maximum records the bank offset. Note in Extended Data Fig. 6 that we can successfully recover the image displacements that are more than 5–10 times smaller than the pixel size.

The computational cost of 2D cross-correlation is $\mathcal{O}(n^4)$, in which n is the width of the image chip. Thus, performing the 2D cross-correlation for every bank position along the river of interest (Fig. 1) is computationally expensive and difficult to scale to larger rivers, longer time series or higher-resolution imagery. Thus, we make use of the convolution theorem (that is, the fact that convolution in the spatial domain is equivalent to multiplication in the Fourier domain)[46]. Convolution between two images is equivalent to correlation if the intensity values of one of the images are rotated 180°. Thus, the 2D cross-correlation between two images, $\mathbf{I}_1$ and $\mathbf{I}_2$, is:

$$\mathbf{Q}(\omega_x, \omega_y) = \mathcal{F}(\mathbf{I}_1(x,y)) \odot \mathcal{F}(\mathbf{I}_2(x,y))^{\star} \tag{16}$$

in which $\mathbf{Q}(\omega_x, \omega_y)$ is the cross-correlation spectrum, $\mathcal{F}$ represents the (2D) Fourier transform, $\odot$ represents element-wise multiplication and * denotes the complex conjugate[31,47]. In practice, weighting the complex-valued spectrum $\mathbf{S}_1(\omega_x, \omega_y) = \mathcal{F}(\mathbf{I}_1(x,y))$ by a tapered filter such as a raised cosine filter[31], $\mathbf{V}$, helps to reduce the influence of the image borders and suppress high-frequency components of the spectrum[31,47].

To measure the migration of a riverbank between two images, we generate two image 'chips' (small $n \times n$-pixel windows, centred at the bank margin for the region of interest). These two image chips have the same geographic coordinates. We then take the Fourier transform of

each chip, weight each spectrum using a raised cosine filter (**V**), take the complex conjugate of the weighted spectrum for the search image (image 2) and multiply the resulting signals in the frequency domain:

$$\mathbf{Q}(\omega_x, \omega_y) = (\mathbf{V}_1 \odot \mathcal{F}(\mathbf{I}_1(x, y))) \odot (\mathbf{V}_2 \odot \mathcal{F}(\mathbf{I}_2(x, y)))^{\star} \quad (17)$$

Note that some care must be taken in choosing the window size (n) of the image chips, which we discuss below. The results of the Fourier methods shown in Extended Data Fig. 6 are numerically equivalent to those produced by the computation of the 2D cross-correlation in the spatial domain. However, the Fourier methods are much faster.

Qualitatively, there are two insights from our algorithm. The first is that the common methodology of thresholding to produce binary river masks[10,20,29] removes most of the information encoded in the image; retaining the image spectral information as continuous values enables the measurement of small bank displacements because we can use spectral unmixing to estimate the relative proportions of the different ground cover types (for example, river versus floodplain) that comprise an individual pixel. The second insight is that feedbacks between erosion and river flow[48,49] mean that bank erosion rates should have a high degree of spatial autocorrelation (Fig. 1). In other words, the bank erosion rate at one location should be similar to the erosion rate at some distance d away, as long as d is smaller than the channel width W (refs. 39,48,49). As a result, averaging observations across neighbouring pixels can improve the signal-to-noise ratio and yield more robust bank displacement estimates. Our Fourier methods do this spatial averaging implicitly, as the whole length of the river margin in the $n \times n$-pixel image chip is used to calculate the bank migration. Intuitively, because the Fourier methods convert from the spatial domain to the frequency domain, our detection limit for bank migration becomes limited by the frequency content of the transformed images, which depends on the width n of the image chip[31,46].

Selecting the window size (n). The choice of n reflects a balance between the spatial resolution (that is, localizing a bank change estimate to a small segment of the riverbank) and the spectral amplitude, which translates to the precision of the (Δ_x, Δ_y) bank offset estimate). There are several considerations in the choice of n. On one hand, n should be small enough that bank offsets, (Δ_x, Δ_y), are uniform across the window. If the image chip is so large that it includes a meander bend for example, the magnitude and direction of bank change will vary across the image chip and the displacement estimate using equation (17) will be a poor representation of local estimates of bank migration. On the other hand, n must be large enough that signal (image texture representing real differences in ground reflectance), rather than noise, is matched between image pairs. Having larger n also allows for greater spectral amplitude and therefore higher precision in the displacement estimate. In practice, Leprince et al.[31] find that $n = 32$ pixels reflects a good balance between obtaining high-spatial-resolution offset estimates (a consideration that favours low n) and having both sufficient signal in the image chips and sufficient spectral resolution to make accurate and precise phase offset measurements (a consideration that favours high n). The value of n also controls the minimum channel size for which we can obtain robust single-bank erosion estimates. For example, a chip of $n = 32$ pixels, centred on the bank margin, typically will not capture the opposing riverbank or other side of a meander bend for channels greater than about 16 pixels in width (Extended Data Fig. 6). For images with 3.0-m spatial resolution (images from the PlanetScope constellation), this 16-pixel constraint corresponds to channels that are 48 m wide.

Remote-sensing datasets. For observing the spatial pattern of bank erosion (Extended Data Fig. 9), we use a pair of Sentinel-2 images (10-m spatial resolution), spaced 6 years apart (30 August 2016 and 13 July 2022) (Extended Data Fig. 6). For reconstructing the sub-seasonal pattern of bank erosion, we require higher spatial resolution, so we use PlanetScope satellite imagery (3.0-m spatial resolution, 16-bit radiometric resolution) from Planet Labs (https://www.planet.com/). We compile 61 daily image mosaics acquired over the period 2016–2022, for an average of about ten cloud-free image observations for each season (the period from May until late October, when the river is unfrozen). See Supplementary Table 1 for a list of PlanetScope observation dates.

Image pre-processing. A notable challenge in the detection of riverbank erosion on seasonal timescales is ensuring that changes in river stage (water level) are not misinterpreted as bank migration. Extended Data Fig. 6 shows an example of how falling river level over the course of the 2022 summer season affects the appearance of the riverbank in true-colour (RGB) imagery. If these unprocessed true-colour composites were used as the input to the sub-pixel offset mapping algorithm (see above), we would inadvertently track the changing water line rather than the eroding riverbank. Therefore, as a first pre-processing step, we transform the images shown in Extended Data Fig. 6 using the normalized difference vegetation index (NDVI) band ratio:

$$\mathrm{NDVI} = \frac{\mathrm{NIR} - \mathrm{R}}{\mathrm{NIR} + \mathrm{R}} \quad (18)$$

in which NIR and R represent the intensity values associated with the near-infrared and red bands of light, respectively. The NDVI is principally sensitive to the presence of vegetation, rather than the presence of water. Notice in Extended Data Fig. 6 that exposed sand bars and water have relatively similar NDVI values. Thus, the primary intensity gradients in the NDVI images are between the vegetated riverbank and the channel (which, depending on the river stage, can consist of sand or water).

The NDVI values of the river and surrounding vegetated banks vary from image to image as a function of the water turbidity, the seasonal changes in vegetation (for example, the greening 'leaf-out' period in the spring and autumnal senescence in the fall) and atmospheric conditions that affect the relative intensities of light measured in the near-infrared versus red wavelengths of light. However, regardless of these seasonal changes and atmospheric correction effects, it is always true that the strongest gradient in the NDVI images is between the vegetated riverbank and the active channel (Extended Data Fig. 6). Therefore, as a second pre-processing step, we fit a simple two-component Gaussian mixture model to the distribution of NDVI values in each image to differentiate the vegetated floodplain from the unvegetated channel. Finally, we compute the image gradient of the fuzzy-classified map generated from the Gaussian mixture model to highlight the location of the riverbank. These image gradient maps are the input to the sub-pixel image-correlation algorithm described above.

Channel identification. We developed an automated pipeline for channel extraction and the identification of riverbanks from satellite imagery. The pipeline uses a combination of thresholding, morphological opening operations and skeletonization. It is implemented in MATLAB (see 'Code availability'). Briefly, the NDVI is calculated following equation (18) and then the image is thresholded to the 10th percentile of the NDVI. The result is a binary mask that separates unvegetated pixels (principally rivers and lakes) from the other pixels. Next, we perform a morphological opening operation (with a disk-structuring element of size 5 pixels = 50 m) to eliminate the small channels from the binary water mask. We then identify the river from the other water features (for example, lakes) in the water mask using a connected-component analysis. Finally, we identify the river centreline by skeletonizing the river mask.

Calculating river curvature. We follow ref. 24 and compute channel curvature (which is the inverse of the radius of curvature, R) as:

$$\frac{1}{R} = \frac{x'y'' - y'x''}{(x'^2 + y'^2)^{3/2}} \quad (19)$$

in which x' and x'' represent the first-order and second-order derivatives of x, respectively. In equation (19), we use the x and y coordinates of the channel centreline, extracted at 10-m intervals and smoothed with a Savitzky–Golay finite impulse response smoothing filter[24,50] with polynomial order 3 and frame length of 33. The frame length is chosen on the basis of the chip width, $n = 32$, plus 1 to ensure that the frame length is an odd integer[50]. Note that the curvature (equation (19)) has units of m^{-1}. We multiply the curvature in equation (19) by the channel width to obtain the local 'normalized curvature' (see equation (25)), which is dimensionless.

Extracting robust erosion rates from noisy time series

We perform the sub-pixel riverbank offset detection algorithm described in Extended Data Fig. 6 between every successive pair of images in the PlanetScope time series. The result is a 61-element 1D time series of inferred bank displacements for each eroding bank location along the Koyukuk River. Note that, although our algorithm can detect riverbank displacements on the order of one-tenth the pixel size (0.3 m), the reported uncertainty in the georeferencing of the PlanetScope images is <10 m root mean square error (typically <5 m root mean square error) (https://www.planet.com/). Therefore, if uncorrected, image-to-image co-registration errors can overwhelm the signal of riverbank erosion.

To obtain more robust erosion rates from the PlanetScope time series, we make use of the fact that the Fourier methods (Extended Data Fig. 6) are so computationally efficient that it is tractable to measure the bank displacements not just between successive images, but between every image to every other image. Thus, instead of 61 pairwise comparisons (in which the first image is compared with itself), we perform $61 \times 61 = 3{,}721$ pairwise comparisons. Although this decision makes the computational cost of performing the time-series analysis scale like $\mathcal{O}(m^2)$ rather than $\mathcal{O}(m)$, in which m is the number of images, the advantage of this approach is that it allows us to perform two types of filtering—stacking and bracketing—that help us see through the noise of image-to-image co-registration errors and extract robust erosion records.

The pairwise bank displacements computed from each image to every other image can be visualized in matrices such as that in Extended Data Fig. 7. In the matrix $E(x, y)$ shown in Extended Data Fig. 7, each row (y) represents a different template image and each column (x) represents a different search image. Along the diagonals, images are compared with themselves, so the estimated offsets are 0. The triangles on either side of the matrix diagonal are mirror images of each other (related through a negative sign):

$$E(x, y) \approx -E(y, x) \quad (20)$$

For example, position (1, 40) compares image 1 as the reference image to image 40 as the search image, whereas position (40, 1) compares image 40 as the reference image to image 1 as the search image. In principle, the approximate equality in equation (20) should be exact. However, because we follow ref. 31 and use different taper functions for the template and search images ($\mathbf{V}_1$ and $\mathbf{V}_2$ in equation (17)), $E(x, y)$ and $-E(y, x)$ can differ slightly from each other. When $E(x, y)$ and $-E(y, x)$ diverge substantially, the bank offset measurement is not robust and we reject the measurement. Thus, computing $E(x, y)$ and $-E(y, x)$ separately is a way to detect and remove outliers.

As a simple experiment to illustrate how we handle the data in $E(x, y)$, we create a synthetic time series of riverbank erosion based on the discharge climatology for the Koyukuk River (Extended Data Fig. 1a) and the model for entrainment-limited erosion (equation (6)). Extended Data Fig. 7c shows the instantaneous erosion rate and Extended Data Fig. 7d shows the cumulative bank displacement from 2016 to 2022. We then sample the cumulative displacement curve at the times of our PlanetScope image acquisitions. The matrix in Extended Data Fig. 7e shows the bank offsets extracted from this synthetic, noise-free dataset. The blocky appearance of the displacement matrix is the result of the limited temporal resolution of our image time series. Note that the bank offsets in Extended Data Fig. 7e change monotonically with time. Our real (noisy) data have non-monotonic jumps, which are largely the result of co-registration errors (Extended Data Fig. 7f). Our goal is to find the most probable monotonic erosion record that underlies (gives rise to) our noisy observations. We achieve this through: (1) stacking; (2) bracketing; and (3) Markov chain Monte Carlo (MCMC) simulations.

Stacking. Each row of the matrix $E(x, y)$ represents the time series of bank displacements constructed by comparing each image in the PlanetScope dataset (see Supplementary Table 1) (the 'search' image) to the same 'template' image. For example, the first row of Extended Data Fig. 7e compares every image to the image acquired on 31 August 2016. The second row compares every image to the image acquired on 4 September 2016 and so on. Thus, averaging the relative displacement sequences encoded by each row of $E(x, y)$ (which we refer to here as stacking) helps to reduce noise associated with co-registration errors in the template image.

Bracketing. Note that co-registration errors in the search image are not reduced by the stacking procedure above, as each column of $E(x, y)$ has the same search image (so every row being stacked has the same co-registration error in the x position of $E(x, y)$). To make the reconstructed displacement time series more robust to errors in the search image co-registration, we compute the cumulative displacements through each row of $E(x, y)$ while skipping every other column, every two columns, every three columns, every four columns and so on. Thus, the estimated cumulative displacement at any time t in the time series is bracketed by displacement estimates that were made from the images surrounding the image acquired at time t but not from that image at time t itself.

MCMC sampling to identify monotonic paths through the bank-position time series. Finally, we impose the constraint that the cumulative displacement record should be a monotonic function of time. The assumption here is that—in most cases—a riverbank should not transition from eroding to accreting over the course of our 6-year observational window. Thus, non-monotonic back-stepping of the bank position is most probably the result of unmitigated co-registration errors (Extended Data Fig. 7h). We seek the most probable monotonic path through the cumulative displacement time series (Extended Data Fig. 7h). This problem is similar to the task of constructing a geological age model for a sequence of stratigraphic layers[51–54]. Steno's principle of superposition states that each successive stratigraphic layer should be younger than the one before it. This geological constraint helps us reduce the uncertainties of depositional ages of horizons dated using radioisotopic measurements[51]. In the example of constructing a geological age model, we can perform a random walk through the sequence of radioisotopic ages (which are a function of height in a stratigraphic column) with the constraint that the age can either get younger or stay the same—but not get older—as we move our way up the stratigraphic column[51–54]. We perform the same type of procedure using our cumulative displacement time series (Extended Data Fig. 7i).

Identification and removal of seasonal biases using measured displacements at slowly eroding banks. As shown in Extended Data Fig. 6, a critical step in our workflow is the transformation of the original

multispectral image (RGB-NIR) to a greyscale image that accentuates the image gradient at the channel–floodplain boundary. This spectral transformation should mute the variation in image intensity resulting from changes in water turbidity, river stage, soil water content and so on over the course of the season, such that the position of the channel–bank boundary is always the strongest feature (contrast) in the image. We find that the NDVI (equation (18)) is a simple band transformation that accomplishes this goal (Extended Data Fig. 6). However, to ensure that changes in water level or vegetation greenness and so on do not bias the results of our seasonal reconstructions of erosion rates (Extended Data Fig. 7), we compute the bank offset matrix for all relatively 'static' bank locations along the 450-km reach of the Koyukuk River (Extended Data Fig. 9), defined as those banks that have eroded or accreted <1 m over the 6-year time series. Displacements from co-registration errors (the $\{\Delta x, \Delta y\}$ shifts from image to image) largely cancel out by stacking the displacement observations from many banks (see Supplementary Fig. 1). However, inferred displacements caused by water-level drops for example will not disappear during stacking, because a water-level drop would be measured as bank accretion no matter what orientation the riverbank is in (Supplementary Fig. 1). Therefore, seasonal patterns of erosion/accretion in our stacked dataset from all slowly eroding/accreting banks probably reflect seasonal biases in our detection of the channel–floodplain boundary and are therefore removed from our displacement matrix:

$$E_{cor}(x,y) = E_{orig}(x,y) - E_{slow}(x,y) \tag{21}$$

in which $E_{cor}(x, y)$ is the corrected pairwise displacement matrix, $E_{orig}(x, y)$ is the original (uncorrected) pairwise displacement matrix and $E_{slow}(x, y)$ is the stacked pairwise displacement matrix for all slowly eroding/accreting banks (≤1 m of change detected over our 6-year observational window).

Capturing the spatial pattern of riverbank erosion

Phenomenological models for river meandering and the 'upstream adjusted curvature'. It has long been observed from field[55–58], laboratory[59] and remote-sensing[24,60] observations that the rate of riverbank erosion is not constant along a meandering river but instead focused at the river bends[57]. This spatial focusing of river migration rate is the result of stress gradients developed between the inner and outer edges of a meander bend, which drive differential erosion and deposition of sediment[49,56,58,61,62]. The first field observations suggested that there was a non-monotonic relationship between river curvature and migration rate[57]; migration rates peaked when the radius of curvature is two to three times the channel width[57]. This relationship was reproduced in subsequent studies[63–66]. However, as pointed out by Furbish[40] and others, comparing bank erosion rates to the local river curvature (Extended Data Fig. 9) neglects the cumulative aspect of how river curvature affects near-bank shear stresses[40]. River curvature must be sustained for some distance in order for the high-velocity filament of flow in the river channel to be displaced towards the outer bend, increasing the local velocity gradient and thus the shear stress on the outer bank[40,42,49]. Thus, two river bends with the same radius of curvature can have different migration rates[40]. Likewise, the bank erosion rate at the entrance to a bend should be less than the migration rate at the downstream side of the bend[40] (Fig. 1f). This cumulative behaviour of river curvature is captured empirically/phenomenologically by convolutional models such as the model of Howard and Knutson[39]. The bank migration rate, $M(s)$, is modelled as:

$$M(s) = \Omega M_0(s) + \left(\Gamma \int_0^\infty M_0(s-\zeta)G(\zeta)\mathrm{d}\zeta\right)\left(\int_0^\infty G(\zeta)\mathrm{d}\zeta\right)^{-1} \tag{22}$$

in which s is the along-river coordinate system (longitudinal distance), ζ is the distance upstream from the point of interest and $G(\zeta)$ is a weighting function that decays exponentially upstream from the point of interest:

$$G(\zeta) = \mathrm{e}^{-\alpha\zeta} \tag{23}$$

The α term in equation (23) controls the rate of decay of the influence of the upstream curvature and it can be parameterized as a function of the friction factor, C_f (dimensionless), and the water depth, H (m) (refs. 24,39):

$$\alpha = 2C_f/H \tag{24}$$

The term $M_0(s)$ represents what Howard and Knutson[39] refer to as the 'nominal' migration rate, that is, the rate that would be observed if migration were only a function of local curvature. The simplest functional dependence for $M_0(s)$ is[39]:

$$M_0(s) = k\left(\frac{W}{R}\right) \tag{25}$$

in which k (m yr^{-1}) is a migration rate constant, W (m) is the channel width and R (m) is the local radius of curvature. We refer to the dimensionless ratio W/R as the 'local normalized curvature'. In equation (22), Ω and Γ are constants (−1 and 2.5, respectively)[39].

The intuition underlying the Howard and Knutson[39] model (equation (22)) is the same as that shown in the cartoon in Fig. 1f; the river migration rate depends not only on the local curvature but also on the river curvature upstream of the point of interest. However, the influence of the neighbouring curvature declines as we move farther from the point of interest. This intuition is confirmed by theoretical models in which bank erosion is considered to be a linear function of the near-bank excess velocity, which can be approximated using the shallow water equations[49].

Accounting for the cumulative effects of curvature rather than just the local curvature makes the sigmoidal relationships shown in Extended Data Fig. 9c–f reduce to a simple first-order (quasi-linear) relationship[24,60] between the bank erosion rate, E (m yr^{-1}), and what we refer to as the 'lag-adjusted dimensionless curvature'[24,60] (Extended Data Fig. 9h–l). The lag-adjusted dimensionless curvature (C) is defined using the convolutional formulation of Howard and Knutson[39] (equations (22)–(25)):

$$C = \Omega\left(\frac{W}{R}\right) + \left(\Gamma \int_0^\infty \left(\frac{W}{R}\right)(s-\zeta)G(\zeta)\mathrm{d}\zeta\right)\left(\int_0^\infty G(\zeta)\mathrm{d}\zeta\right)^{-1} \tag{26}$$

Equation (26) simply modifies the local normalized curvature (W/R) by the weighting function $G(\zeta)$ that decays exponentially upstream from the point of interest. On the basis of equation (22), the bank migration rate, M, is a simple linear function of the lag-adjusted dimensionless curvature (C):

$$M = kC \tag{27}$$

in which k (m yr^{-1}) is the same migration rate constant as in equation (25). In Figs. 1 and 2, we compute the lag-adjusted dimensionless curvature (C) (equation (26)) using measurements of river width and river curvature. We then compare C with the observed migration rates to quantify k. The quantity k conveys how fast river migration proceeds for a given amount of river curvature. This parameter thereby removes the first-order control of river geometry (curvature) in setting local river migration rates[24] (Figs. 1 and 2) and highlights the role of bank material properties.

Field evaluation of near-surface permafrost map. To evaluate the accuracy of the Pastick et al.[32] Alaska-wide permafrost map for our study

area along the Koyukuk River (Fig. 2), we used a permafrost probe to collect $n = 176$ permafrost presence/absence and active layer thickness observations during field expeditions to the Koyukuk River in July 2018 ($n = 137$), June 2022 ($n = 2$) and October 2022 ($n = 37$)[67] (Extended Data Fig. 8). Our ground-truth observations suggest that applying a simple classification threshold value of 40% to the Pastick et al.[32] permafrost probability map can identify permafrost presence/absence with an average accuracy of 69% (Extended Data Fig. 10).

Data availability

The Sentinel-2 satellite images used to extract the 2016–2022 migration rates shown in Fig. 1 are freely available from the European Space Agency on data portals such as the Copernicus Open Access Hub (https://scihub.copernicus.eu/). The PlanetScope images used for the seasonal time-series analysis (Fig. 3) are available from Planet Labs (https://www.planet.com). The stream gauge data in Extended Data Fig. 2 are available from the United States Geological Survey (https://waterdata.usgs.gov/nwis). The permafrost map used in Fig. 2 and Extended Data Fig. 10 is from ref. 32 and is made available by the United States Geological Survey (https://www.sciencebase.gov/catalog/item/5602ab5ae4b03bc34f5448b4). Our spatial measurements of riverbank erosion from the Sentinel-2 and PlanetScope time-series analysis (Figs. 1–3) are packaged on the NSF Arctic Data Center[68]: https://doi.org/10.18739/A2HM52M6Q. Our field observations of permafrost presence/absence (Extended Data Fig. 10) from summer 2018 and fall 2022 are published on the ESS-DIVE repository[67] (https://doi.org/10.15485/2204419).

Code availability

Our methodology for measuring sub-pixel bank erosion, as well as our workflow for channel extraction and the measurement of channel morphometrics (width, radius of curvature, longitudinal distance and so on) (Fig. 1), is available on the NSF Arctic Data Center[68]: https://doi.org/10.18739/A2HM52M6Q. The code is written in MATLAB.

41. Vanoni, V. A. & Brooks, N. H. *Laboratory Studies of the Roughness and Suspended Load of Alluvial Streams* (California Institute of Technology Sedimentation Laboratory, 1957).
42. Kean, J. W. & Smith, J. D. in *Riparian Vegetation and Fluvial Geomorphology* Vol. 8 (eds Bennett, S. J. & Simon, A.) 237–252 (American Geophysical Union, 2004).
43. Li, T., Venditti, J. G., Rennie, C. D. & Nelson, P. A. Bed and bank stress partitioning in bedrock rivers. *J. Geophys. Res. Earth Surf.* **127**, e2021JF006360 (2022).
44. Ferguson, R. I., Hardy, R. J. & Hodge, R. A. Flow resistance and hydraulic geometry in bedrock rivers with multiple roughness length scales. *Earth Surf. Process. Landf.* **44**, 2437–2449 (2019).
45. Douglas, M. M. & Lamb, M. P. A model for thaw and erosion of permafrost riverbanks. *J. Geophys. Res. Earth Surf.* **129**, e2023JF007452 (2024).
46. Leprince, S. *Monitoring Earth Surface Dynamics With Optical Imagery*. PhD thesis, California Institute of Technology (2008).
47. Altena, B. & Leinss, S. Improved surface displacement estimation through stacking cross-correlation spectra from multi-channel imagery. *Sci. Remote Sens.* **6**, 100070 (2022).
48. Parker, G. et al. A new framework for modeling the migration of meandering rivers. *Earth Surf. Process. Landf.* **36**, 70–86 (2011).
49. Ikeda, S., Parker, G. & Sawai, K. Bend theory of river meanders. Part 1. Linear development. *J. Fluid Mech.* **112**, 363–377 (1981).
50. Savitzky, A. & Golay, M. J. Smoothing and differentiation of data by simplified least squares procedures. *Anal. Chem.* **36**, 1627–1639 (1964).
51. Schoene, B. et al. U-Pb constraints on pulsed eruption of the Deccan Traps across the end-Cretaceous mass extinction. *Science* **363**, 862–866 (2019).
52. Keller, C. B. Chron.jl: a Bayesian framework for integrated eruption age and age-depth modelling. OSF (Open Science Framework) https://doi.org/10.17605/OSF.IO/TQX3F (2018).
53. Schoene, B., Eddy, M. P., Keller, C. B. & Samperton, K. M. An evaluation of Deccan Traps eruption rates using geochronologic data. *Geochronology* **3**, 181–198 (2021).
54. Zhang, T. et al. A Bayesian framework for subsidence modeling in sedimentary basins: a case study of the Tonian Akademikerbreen Group of Svalbard, Norway. *Earth Planet. Sci. Lett.* **620**, 118317 (2023).
55. Fisk, H. N. *Geological Investigation of the Alluvial Valley of the Lower Mississippi River* (U.S. Army Corps of Engineers, 1944).
56. Leopold, L. B. & Wolman, M. G. River meanders. *Geol. Soc. Am. Bull.* **71**, 769–793 (1960).
57. Hickin, E. J. & Nanson, G. C. The character of channel migration on the Beatton River, northeast British Columbia, Canada. *Geol. Soc. Am. Bull.* **86**, 487–494 (1975).
58. Dietrich, W. E., Smith, J. D. & Dunne, T. Flow and sediment transport in a sand bedded meander. *J. Geol.* **87**, 305–315 (1979).
59. Hooke, R. L. B. Distribution of sediment transport and shear stress in a meander bend. *J. Geol.* **83**, 543–565 (1975).
60. Donovan, M., Belmont, P. & Sylvester, Z. Evaluating the relationship between meander-bend curvature, sediment supply, and migration rates. *J. Geophys. Res. Earth Surf.* **126**, e2020JF006058 (2021).
61. Bagnold, R. A. *Some Aspects of the Shape of River Meanders* (US Government Printing Office, 1960).
62. Eke, E., Parker, G. & Shimizu, Y. Numerical modeling of erosional and depositional bank processes in migrating river bends with self-formed width: morphodynamics of bar push and bank pull. *J. Geophys. Res. Earth Surf.* **119**, 1455–1483 (2014).
63. Nicoll, T. J. & Hickin, E. J. Planform geometry and channel migration of confined meandering rivers on the Canadian prairies. *Geomorphology* **116**, 37–47 (2010).
64. Hudson, P. F. & Kesel, R. H. Channel migration and meander-bend curvature in the lower Mississippi River prior to major human modification. *Geology* **28**, 531–534 (2000).
65. Finotello, A. et al. Field migration rates of tidal meanders recapitulate fluvial morphodynamics. *Proc. Natl Acad. Sci.* **115**, 1463–1468 (2018).
66. Hooke, J. River meander behaviour and instability: a framework for analysis. *Trans. Inst. Br. Geogr.* **28**, 238–253 (2003).
67. Douglas, M. et al. Geomorphic mapping and permafrost occurrence on the Koyukuk River floodplain near Huslia, Alaska (ESS-DIVE dataset) (2023).
68. Geyman, E., Avouac, J.-P., Douglas, M. & Lamb, M. Resolving the spatial and seasonal pattern of riverbank erosion on the Koyukuk River, Alaska, 2016–2022. Arctic Data Center (2024).
69. Beltaos, S., Carter, T., Rowsell, R. & DePalma, S. G. Erosion potential of dynamic ice breakup in Lower Athabasca River. Part I: field measurements and initial quantification. *Cold Reg. Sci. Technol.* **149**, 16–28 (2018).
70. Vandermause, R., Harvey, M., Zevenbergen, L. & Ettema, R. River-ice effects on bank erosion along the middle segment of the Susitna river, Alaska. *Cold Reg. Sci. Technol.* **185**, 103239 (2021).
71. Milburn, D. & Prowse, T. D. The effect of river-ice break-up on suspended sediment and select trace-element fluxes: paper presented at the 10th Northern Res. Basin Symposium (Svalbard, Norway – 28 Aug./3 Sept. 1994). *Hydrol. Res.* **27**, 69–84 (1996).
72. Ettema, R. Review of alluvial-channel responses to river ice. *J. Cold Reg. Eng.* **16**, 191–217 (2002).
73. Costard, F., Gautier, E., Fedorov, A., Konstantinov, P. & Dupeyrat, L. An assessment of the erosion potential of the fluvial thermal process during ice breakups of the Lena River (Siberia). *Permafr. Periglac. Process.* **25**, 162–171 (2014).
74. Lininger, K., Wohl, E., Rose, J. & Leisz, S. Significant floodplain soil organic carbon storage along a large high-latitude river and its tributaries. *Geophys. Res. Lett.* **46**, 2121–2129 (2019).
75. Lunardini, V. J., Zisson, J. R. & Yen, Y. C. *Experimental Determination of Heat Transfer Coefficients in Water Flowing over a Horizontal Ice Sheet* (US Army Corps of Engineers, Cold Regions Research & Engineering Laboratory, 1986).

Acknowledgements We thank the Huslia Tribal Council for river and land access and S. Huffman and the Yukon River Inter-Tribal Watershed Council for field and logistical support. We also thank J. Anadu, R. Blankenship, K. Dunne, W. Fischer, Y. Ke, H. Dion-Kirschner, J. Magyar, E. Mutter, J. Nghiem, J. Reahl, R. Rugama-Montenegro, E. Seelen, I. Smith and J. West for help in the field and for fruitful discussions. Planet Labs provided the high-resolution PlanetScope imagery through their Education and Research Program. This work was supported by NSF Award 2127442, NSF Award 2031532, and Caltech's Resnick Sustainability Institute. E.C.G. thanks the NSF Graduate Research Fellowships Program and the Fannie and John Hertz Foundation.

Author contributions E.C.G. and M.P.L. designed the study. M.M.D. and M.P.L. developed the early thermomechanical model. J.-P.A. advised the sub-pixel methodology. E.C.G. developed the sub-pixel methodology, performed the analysis and wrote the manuscript, with input from M.M.D., J.-P.A. and M.P.L.

Competing interests The authors declare no competing interests.

Additional information

Supplementary information The online version contains supplementary material available at https://doi.org/10.1038/s41586-024-07978-w.

Correspondence and requests for materials should be addressed to Emily C. Geyman.

Peer review information *Nature* thanks Evan Dethier, Efi Foufoula-Georgiou and Zoltan Sylvester for their contribution to the peer review of this work. Peer reviewer reports are available.

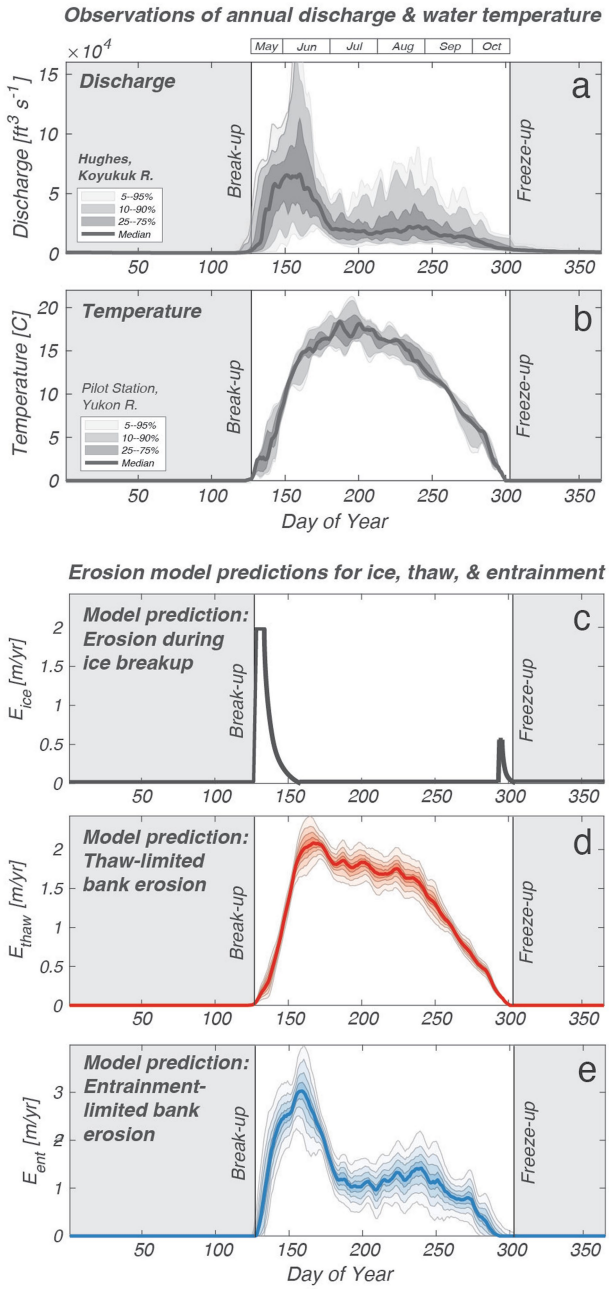

Extended Data Fig. 1 | Discharge and water temperature seasonality on the Koyukuk River (Alaska) and theoretical predictions for the timing of riverbank erosion. a, Discharge climatology for the Koyukuk River at Hughes (66.04696° N, 154.26097° W) based on data from the USGS streamflow station during the period 1962–1981 (Extended Data Fig. 7a). Note that 1 ft^3/s is equal to approximately 0.028 m^3/s. Discharge peaks during the spring freshet in late May to early June. Some years have a second discharge peak associated with August rains (Extended Data Figs. 3 and 7a). The Koyukuk River maintains very low discharge from late October to mid-May, when the surface of the river is frozen. **b**, Average water temperature time series from the USGS gauge at Pilot Station on the Yukon River (61.93369° N, 162.88293° W). The USGS gauge at Hughes does not record water temperature, which is why we rely on the Pilot Station temperature record. However, comparison of water temperatures measured by HOBO loggers deployed on the Koyukuk River near Huslia during the summers of 2022 and 2023 show that the water temperature at Pilot Station is a good proxy for the water temperature on the Koyukuk River. Water temperatures approach 0 °C during the river-ice 'break-up' and 'freeze-up' periods, and peak in mid-July, at a time when the water discharge approaches its summertime low (**a**). **c**–**e**, Theoretical predictions for the sub-seasonal patterns of riverbank erosion under the endmember scenarios that erosion is controlled by: ice gouging during break-up[69–72] (**c**), the thawing of pore-ice in frozen bank sediments[14,26,27,73] (**d**) and the ability for flowing river water to entrain bank sediment[14,36–38] (**e**). The time series in **c** is an illustrative cartoon. The break-up period in May is probably the time of greatest erosive action from ice[21], although the freeze-up period in October can proceed in fits and starts, during which thin ice lenses flow downstream and could erode thawed riverbanks. The uncertainty envelopes in **d** and **e** propagate the discharge and water temperature variability in **a** and **b** using Monte Carlo simulations.

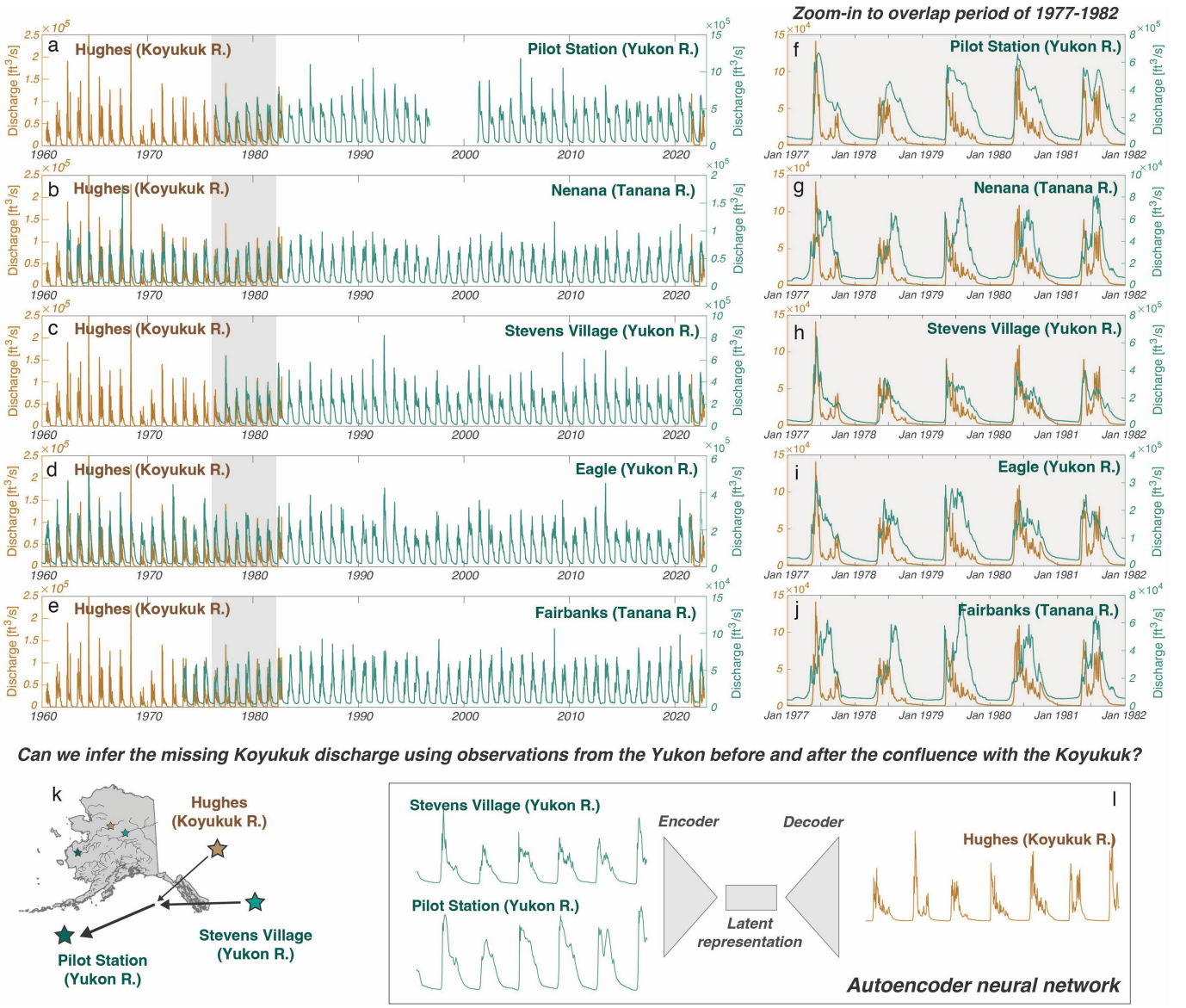

Extended Data Fig. 2 | Illustration and justification for our method of estimating discharge on the Koyukuk River (which is missing gauge data during our study period from 2016 to 2022) based on the discharge time series from nearby rivers. a–**e**, Discharge records from USGS stream gauges at Hughes (66.04696° N, 154.26097° W) (**a**–**e**), Pilot Station (61.93369° N, 162.88293° W) (**a**), Nenana (64.56494° N, 149.09400° W) (**b**), Stevens Village (65.87510° N, 149.72035° W) (**c**), Eagle (64.78917° N, 141.20009° W) (**d**), and Fairbanks (64.79234° N, 147.84131° W) (**e**). Note that 1 ft^3/s is equal to approximately 0.028 m^3/s. The discharge data for the Koyukuk River at Hughes are shown in brown and the discharge data from all other stations are shown in green. **f**–**j**, A zoom-in of the period 1977–1982, when all six stations were recording discharge data. Note the similarity in the hydrographs between the stations. We ask: can we use the historical period of overlap (**f**–**j**) to train a model that infers the discharge on the Koyukuk River given the hydrographs recorded at nearby stations? **k**, Consider the specific case of the streamflow recorded at Hughes, Pilot Station and Stevens Village. The Koyukuk River carries roughly 20% of the streamflow observed on the Yukon River at Stevens Village (**c**,**h**). Thus, the difference in discharge observed at Stevens Village versus Pilot Station (that is, before and after the confluence with the Koyukuk River, respectively) should encode information about the discharge from the Koyukuk River, modulated by a characteristic convolutional smoothing of the hydrograph from upstream to downstream. **l**, We use a simple neural network to infer the hydrograph from the Koyukuk River (which is not directly observed during our study period from 2016–2022) based on the hydrographs of the Yukon River at Stevens Village and Pilot Station (which have continuous observational records from 2016 to 2022). We train the neural network using the period of overlap when all three stations were collecting data from 1977 to 1982 (Extended Data Fig. 3).

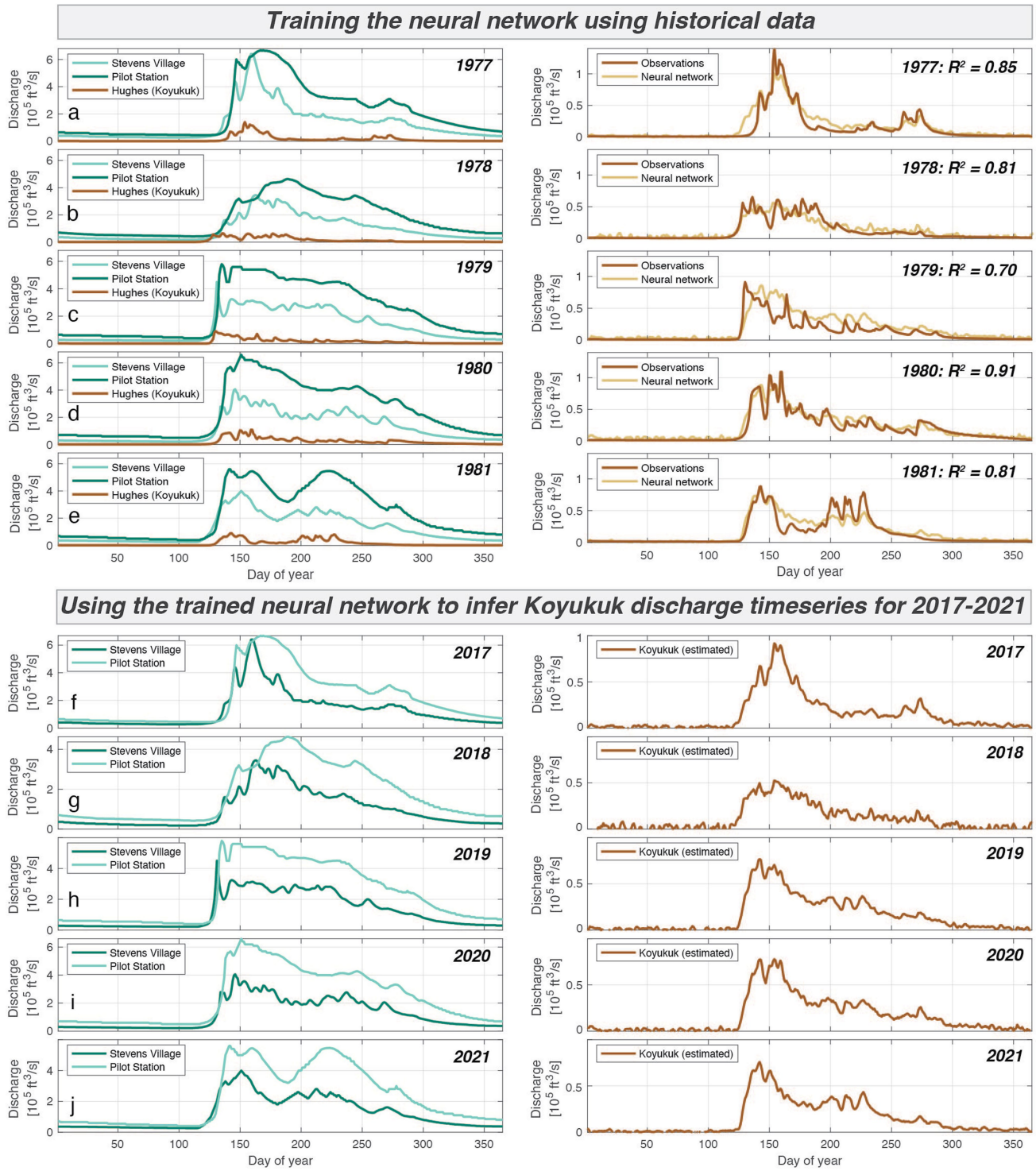

Extended Data Fig. 3 | Training and implementation of our neural network used to infer the 'missing' discharge time series on the Koyukuk River based on the discharge records at Stevens Village and Pilot Station on the Yukon River (before and after the confluence with the Koyukuk River)—see Extended Data Fig. 2. a–e, The neural network is trained using periods of overlap in the historical record when all three USGS streamflow stations were active. In **a–e**, the R^2 values represent the model performance evaluated using leave-one-out cross-validation. The neural network predicts the historical discharge time series with a mean R^2 of 0.82. **f–j**, Implementation of the neural network for estimating the Koyukuk River discharge records during the period 2017–2021. These datasets are used to make model predictions for the seasonal and interannual patterns of riverbank erosion under the thaw-limited, entrainment-limited and combined scenarios (Extended Data Fig. 4).

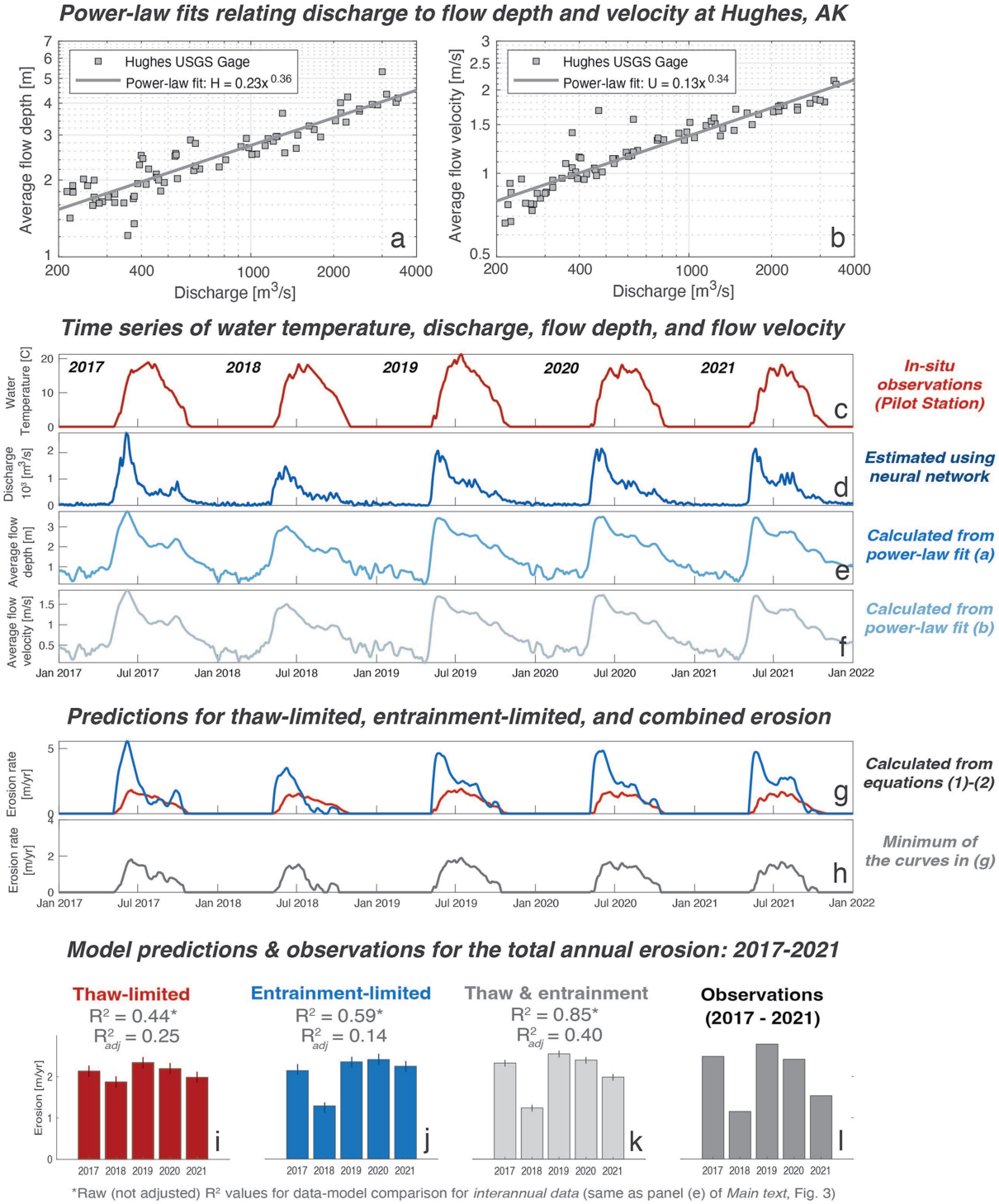

Extended Data Fig. 4 | Time series for quantifying annual erosion rates. **a**,**b**, Power-law regressions relating the water discharge, Q_w, to the average flow depth (H) (**a**) and average flow velocity (U) (**b**) for the USGS station at Hughes. Each data point represents a field measurement from the USGS (mostly from the period 1962–1981). **c**, In situ water temperature observations from Pilot Station on the Yukon River. **d**, Water discharge time series for the Koyukuk River estimated from the neural network in Extended Data Fig. 3. **e**,**f**, Time series of average flow depth (H) and average flow velocity (U) constructed from the discharge dataset in **d** and the power-law fits in **a** and **b**. **g**, Predicted patterns of thaw-limited and entrainment-limited erosion based on equations (3)–(6) and the H and U time series in **e** and **f**. **h**, The minimum of the thaw-limited and entrainment-limited erosion curves in **g**. In **g** and **h**, the y axis gives the instantaneous erosion rate (that is, the total annual erosion that would occur if that rate were sustained for a full 365-day period). **i**–**k**, The integrated areas under the erosion rate curves (**g** and **h**) for thaw-limited (**i**), entrainment-limited (**j**) and combined (**k**) erosion scenarios. **l**, The observed erosion rates for 2017–2021. Note that the model parameters in equations (3)–(6) are optimized separately for each scenario (**i**–**k**) to have the interannual erosion fingerprint best match the observations (**l**) (see Extended Data Fig. 1). Even after optimization, the thaw-limited and entrainment-limited endmembers can only replicate the interannual pattern of erosion with R^2 of 0.44 and 0.57, respectively. The combined thaw and entrainment scenario reproduces the interannual pattern with $R^2 = 0.85$. To account for the fact that the thaw-only, entrainment-only and combined thaw and entrainment models have different numbers of independent parameters (1, 2 and 3, respectively), we also compute the adjusted R^2 value (see equation (15)). The R^2_{adj} metric includes a penalty for models with more parameters, yet it still supports the conclusion that the combined thaw and entrainment model best explains the data.

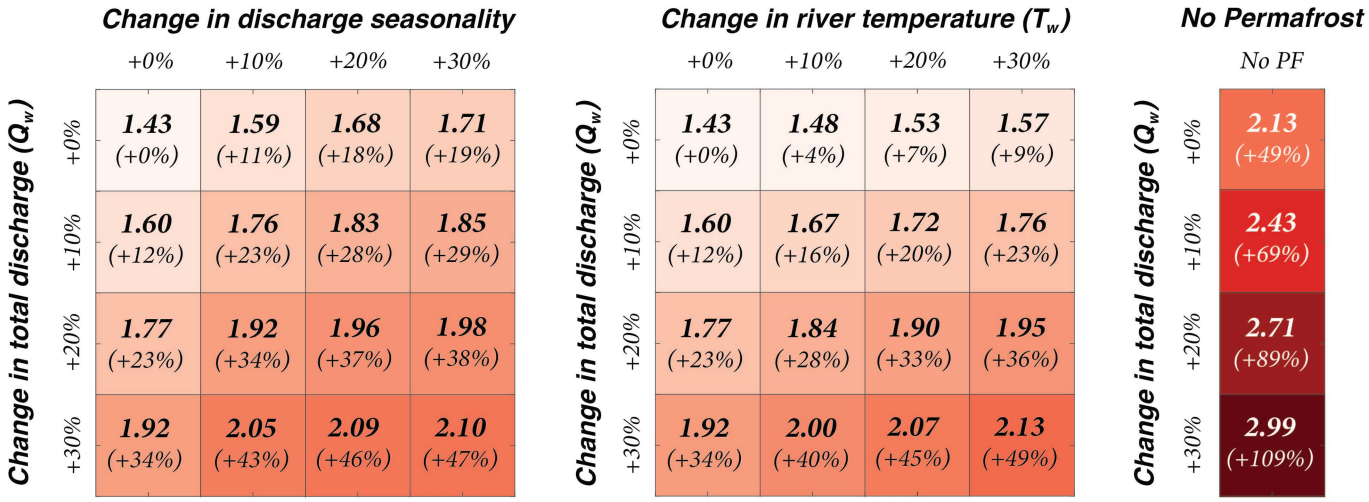

Extended Data Fig. 5 | Simulations for how the reach-averaged riverbank erosion rates for the Koyukuk River may respond to changes in the total water discharge, the discharge seasonality, the water temperature, and the permafrost abundance in the riverbanks. We use the combined thaw-limited and entrainment-limited erosion model (Fig. 3), calibrated using our observations for the seasonal and interannual patterns of bank erosion, to explore changes in erosion rates in response to perturbations in total water discharge (Q_w), discharge seasonality, and water temperature (T_w). Note that our perturbations to the discharge seasonality involve reallocating 0–30% of the water discharge from the first 30 days of ice-free conditions (mid-May to mid-June on the Koyukuk River) to the mid-summer (in this case, to the month of August). This experiment simulates reduced springtime discharge as a result of a smaller snowpack, compensated by increasing summertime rain[8]. Because we lack robust constraints on whether or how the 'flashiness' of the Koyukuk River hydrograph will change, we reallocate the seasonal discharge through simple linear scalings of the historical discharge records (Extended Data Fig. 2). The numbers in bold indicate the reach-averaged bank erosion rates in metres per year and the numbers in parentheses indicate the percent change relative to the modern (2016–2022) erosion rates.

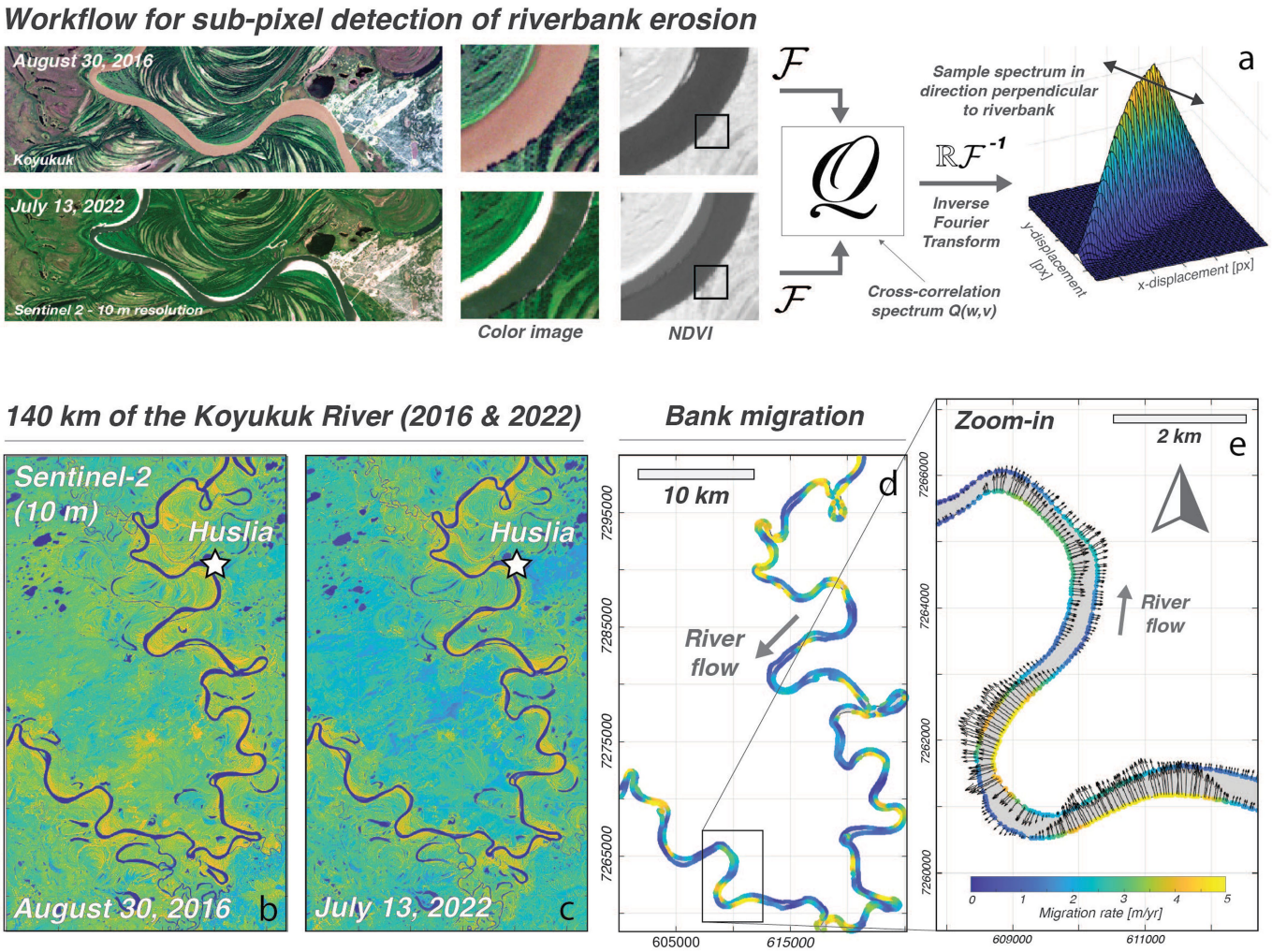

Extended Data Fig. 6 | Methodology for measuring sub-pixel erosion along riverbanks. a, An illustration of the workflow for the sub-pixel detection of riverbank erosion. **b**,**c**, An example of the two Sentinel-2 images used to compute the migration of the Koyukuk River (2016–2022) in Extended Data Fig. 9. The crops in **b** and **c** show a region of the Koyukuk River near Huslia (65.6966° N, 156.3824° W). Note that the river stage and sediment load are higher on 30 August 2016 compared with 13 July 2022, causing the river colour (RGB values) and the position of the land–water boundary to be different in the two images. We want to make sure that our algorithm records the net migration of the river as a result of bank erosion, rather than the variable exposure of sand on the riverbanks resulting from rising and falling river stage. To do so, we transform the multispectral satellite image to the dimensionless NDVI band ratio (equation (18)). The NDVI accentuates the spectral difference between the river water and the vegetated floodplain while collapsing the spectral difference between unvegetated sand and river water. The result is that the NDVI image is relatively insensitive to changes in water level (which expose or submerge unvegetated bars). Next, we extract an $n \times n$-pixel chip, centred at the bank edge for the location of interest, from the image acquired at time 1. We extract an $n \times n$-pixel chip at the same location in the image acquired at time 2. We use Fourier methods to take the 2D cross-correlation of the two image chips. The 2D cross-correlation spectrum, which we upsample by a factor of 10, peaks at a $(\Delta x, \Delta y)$ value that records the estimated riverbank displacement between time 1 and time 2. Note that, given the relatively linear bank geometry (at least on the scale of the $n \times n$-pixel chips), the cross-correlation spectrum has a ridge-like geometry rather than a sharp peak. Thus, when searching for the maximum in the 2D cross-correlation spectrum, we search along a vector that is perpendicular to the orientation of the riverbank (and therefore perpendicular to the ridge in the cross-correlation spectrum). **d**,**e**, Illustration of how we perform the methodology described in **a** for every position along the 450-km reach of the Koyukuk River shown in Fig. 1b.

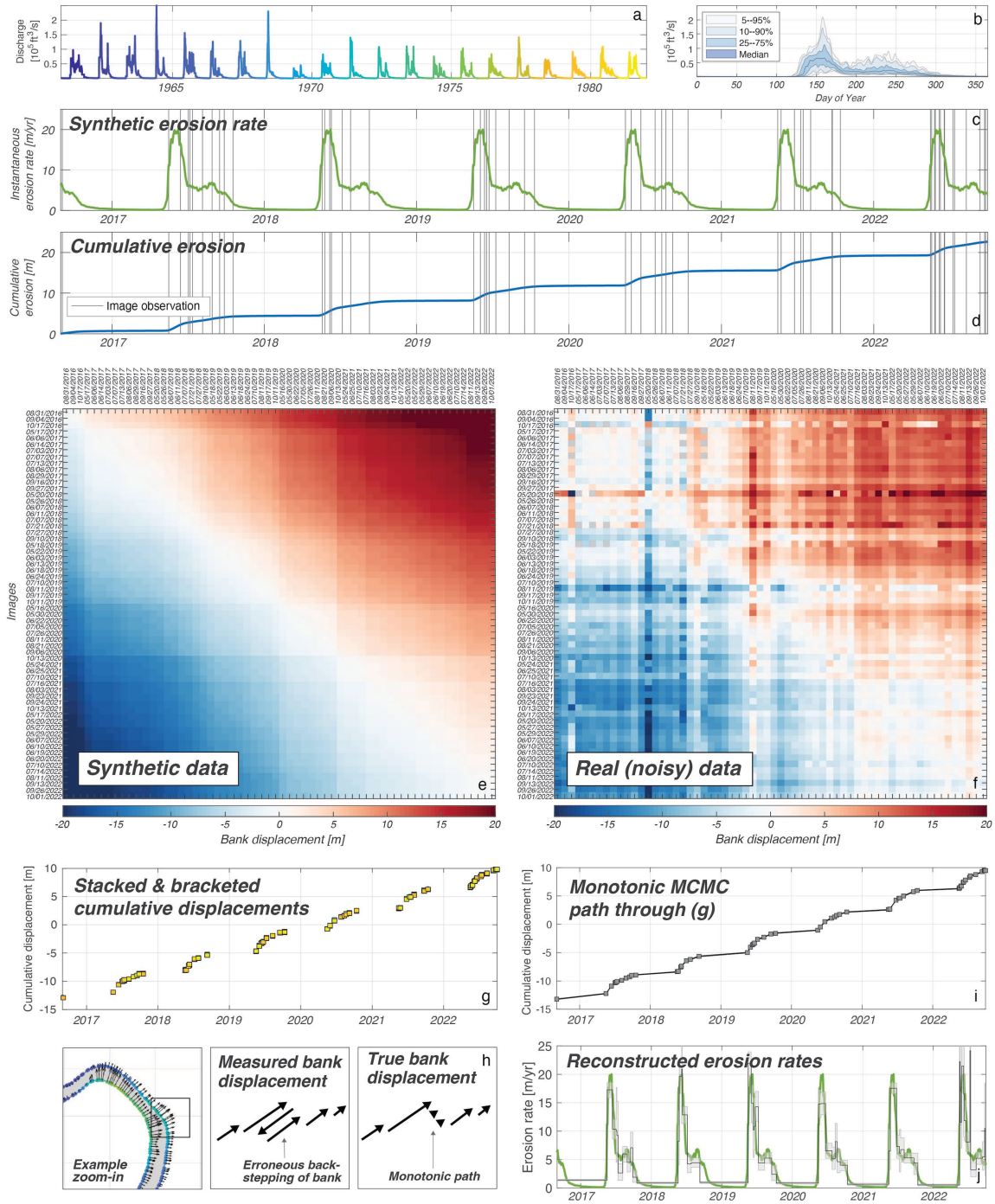

Extended Data Fig. 7 | A synthetic dataset to illustrate our method of reconstructing erosion rates from pairwise bank displacement observations. **a**, Continuous discharge time series for the Koyukuk River from the USGS station at Hughes (1961–1982). **b**, Average annual discharge cycle based on the data in **a**. **c**, A simple synthetic time series for erosion rate based on equation (6) (the entrainment-limited endmember). The 'instantaneous' erosion rate gives the total annual erosion that would occur if that erosion rate were sustained for a 365-day period. The grey lines depict the times for which we have PlanetScope images (see Supplementary Table 1). **d**, The cumulative erosion from the synthetic curve in **d**. **e**, A pairwise displacement matrix computed from the synthetic cumulative erosion curve in **d**. **f**, An example real (noisy) displacement record. **g**, Stacking and bracketing of the displacement matrix leads to less noisy cumulative displacement records. Stacking refers to averaging the differential displacement time series along each column of the matrix in **e**. Bracketing refers to computing the cumulative displacement from every second column, every third column, every fourth column and so on. Stacking (averaging over the rows) makes the cumulative displacement estimates less sensitive to errors in the co-registration of the template image (rows of $E(x, y)$), whereas bracketing (skipping columns) makes the cumulative displacement estimates less sensitive to errors in the co-registration of the search image (columns of $E(x, y)$). **h**,**i**, Remaining noise in the stacked and bracketed cumulative erosion record (**g**) is reduced by imposing the constraint that the cumulative displacement time series should be a monotonic function of time; in most cases, an eroding riverbank should not switch from eroding to accreting over the course of our approximately 6-year analysis. Thus, temporary back-stepping of the bank position (**h**) is probably an error. **i**, We use MCMC to construct the most probable monotonic path through the cumulative displacement time series. **j**, Differentiating the record in **i** with respect to time yields an estimate for the instantaneous erosion rate. The green curve shows the synthetic curve used to generate the displacement matrix (**e**) and the grey curve gives the reconstructed erosion rate (shown as a stair-step plot rather than a continuous curve because our temporal observations are limited to the roughly ten cloud-free PlanetScope mosaics each year (Supplementary Table 1).

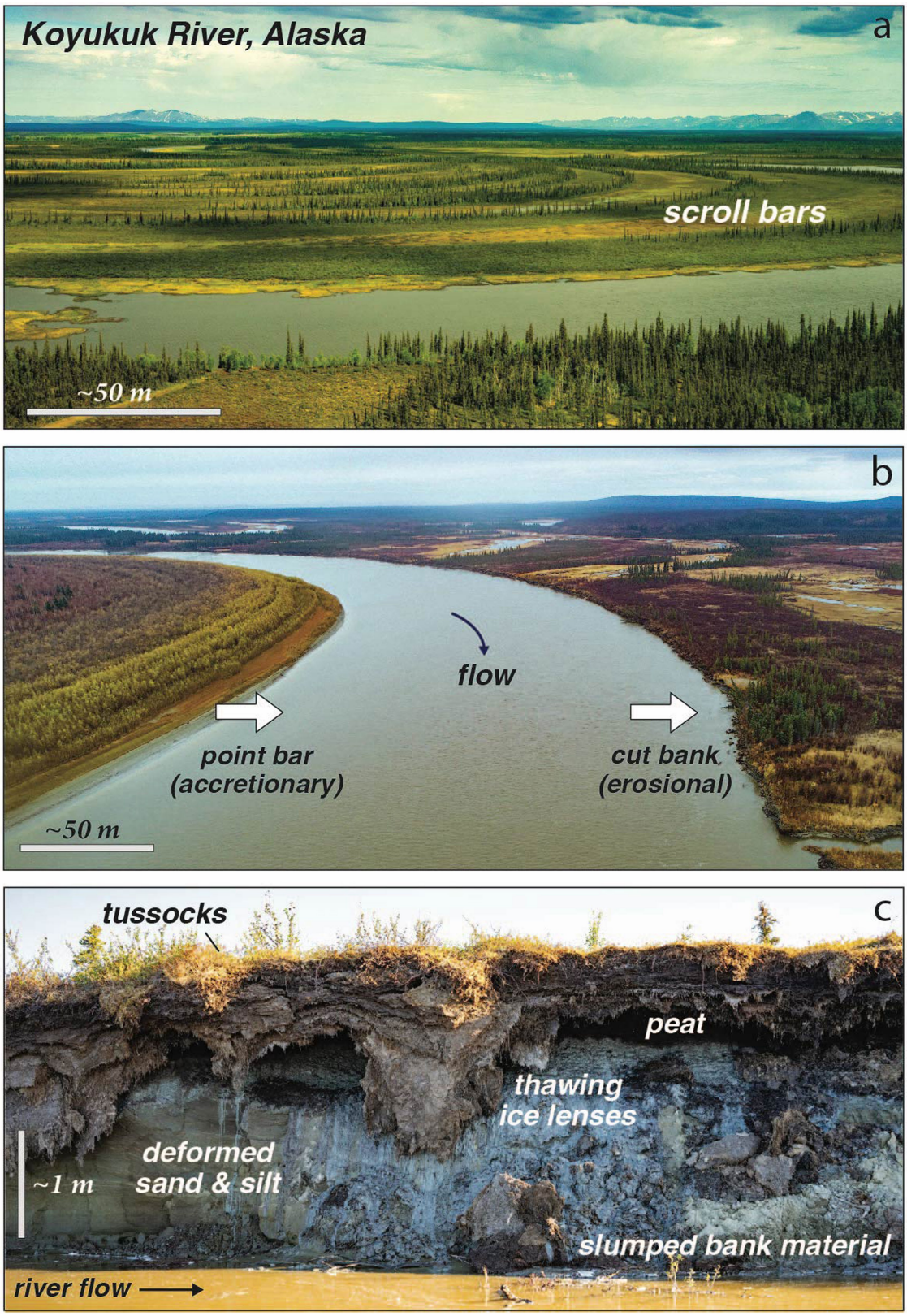

Extended Data Fig. 8 | Representative field photos of the Koyukuk River near Huslia (65.689° N, 156.381° W). a, Scroll bars are arcuate traces of the river's former position recorded in the floodplain landscape. **b**, The inner bend of a channel (point bar) is accretionary, whereas its outer bend (cut bank) is erosional. **c**, A zoom-in on an erosional permafrost cut bank.

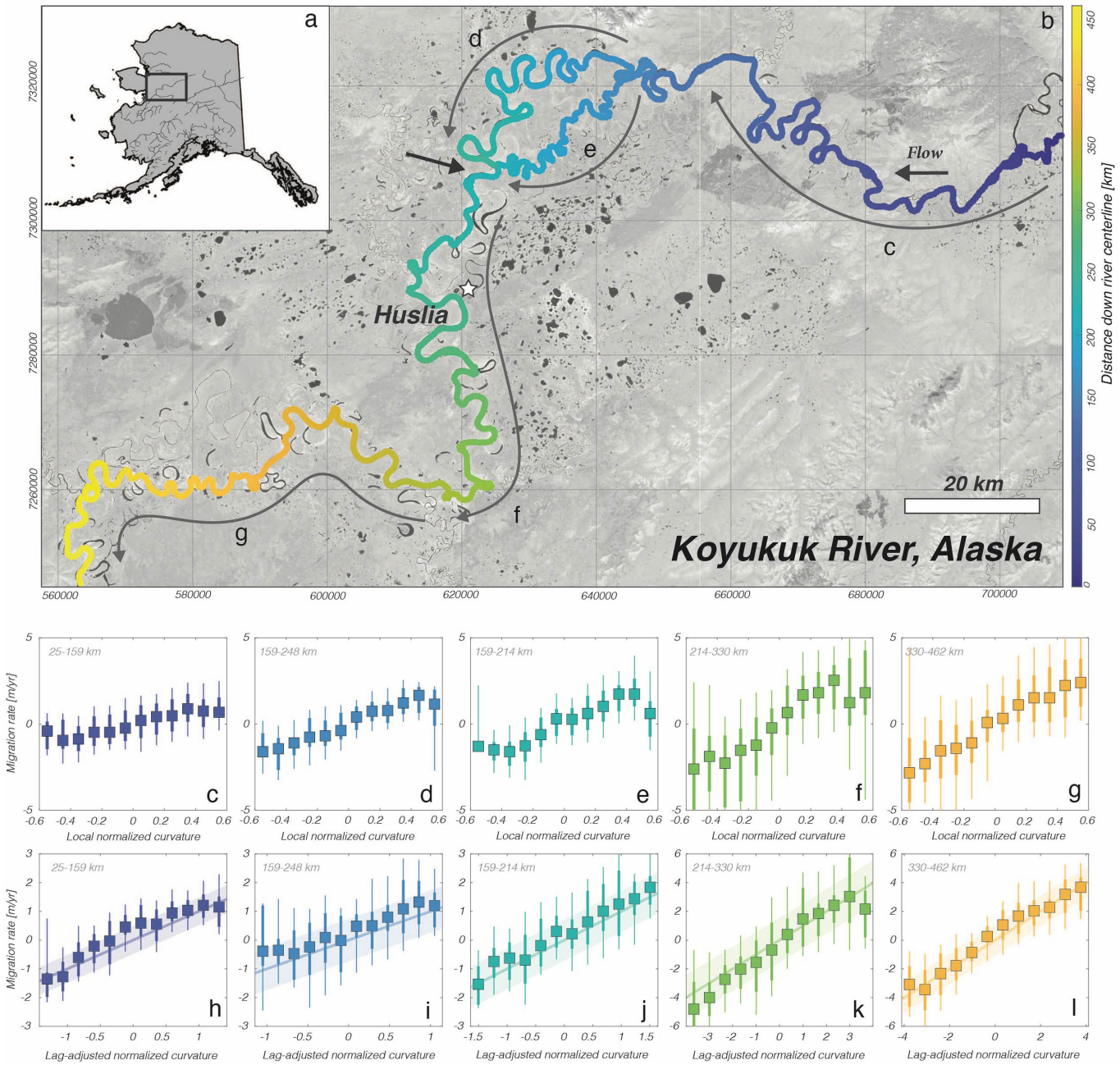

Extended Data Fig. 9 | Spatial patterns of riverbank erosion on the Koyukuk River. This figure is similar to Fig. 1 but it shows the river migration rate as a function of both the local normalized river curvature (W/R, in which W is the river width (m) and R is the local radius of curvature of the channel (m)) (**e**–**g**) and the lag-adjusted normalized curvature, which is given by equation (26) (**h**–**l**). Note that the migration rate saturates at high values of local curvature in **c**–**f**, giving the curvature versus migration rate curves a sigmoidal shape. By contrast, the migration rate is a linear function of the lag-adjusted normalized curvature[24]. Notice that the y-axis scale in **k** and **l** is two times the scale in **h**–**j**. In other words, after the confluence of the two threads of the Koyukuk River at the location indicated by the black arrow in **b**, the curvature-normalized migration rate increases by a factor of 2. As in Fig. 1, the migration rates were measured by applying our sub-pixel offset algorithm to a pair of Sentinel-2 images from 30 August 2016 and 13 July 2022. Here, as in Fig. 1, we quantify the migration rate using the displacement observed on the erosional side of the river (see Fig. 1e).

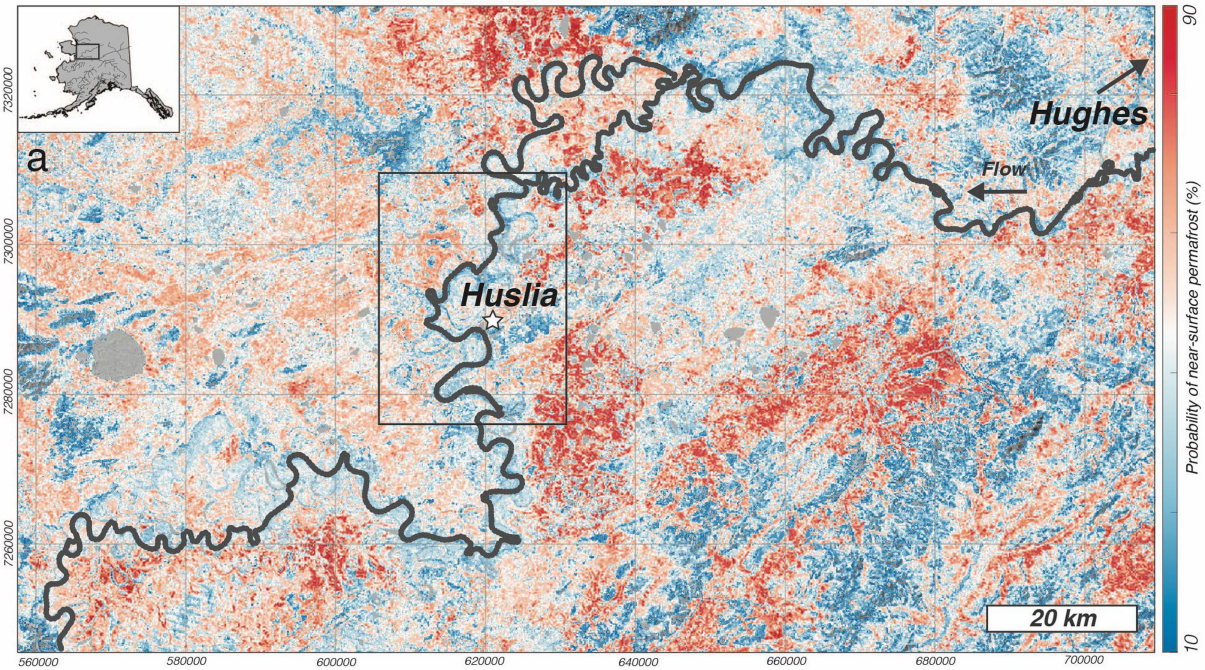

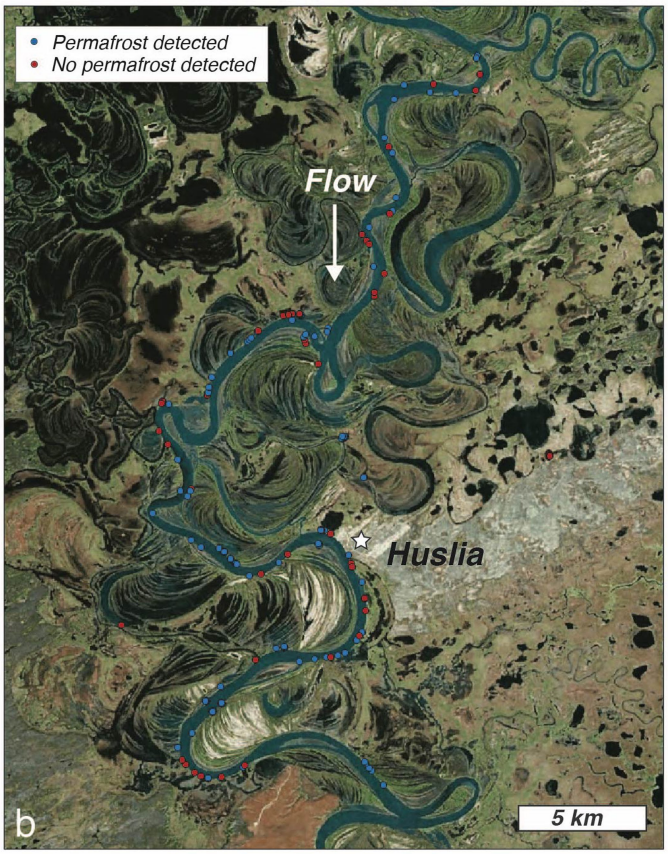

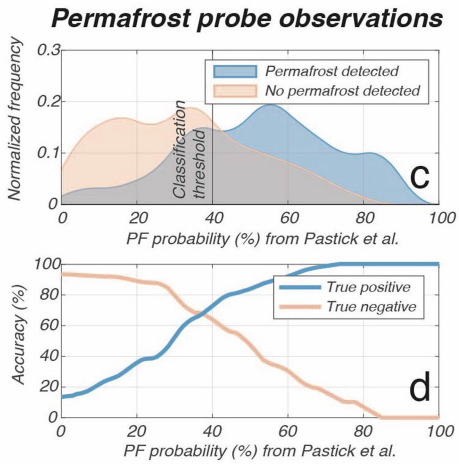

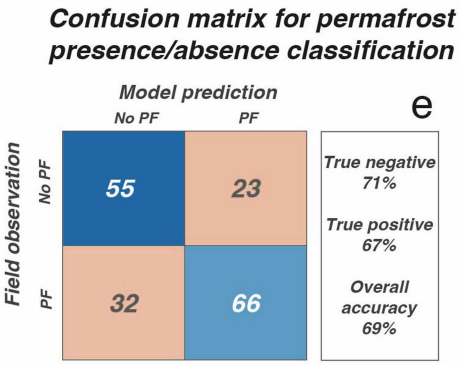

Extended Data Fig. 10 | Field validation of the near-surface permafrost map. a, Probability of near-surface (≤1 m depth) permafrost estimated by Pastick et al.[32]. **b**, Zoom-in to our area of field observations, in which we collected $n = 176$ permafrost probe measurements in July 2018 ($n = 137$), June 2022 ($n = 2$) and October 2022 ($n = 37$). Blue dots indicate permafrost detected and red dots indicate no permafrost detected. **c**, A comparison between our permafrost ground-truth observations (**b**) and the permafrost probability estimates from Pastick et al.[32] (an Alaska-wide permafrost map, calibrated using $n = 16,786$ statewide observations of near-surface permafrost, but no observations in the region shown in **b**). **d**, We explore the accuracy of the Pastick et al.[32] permafrost map for the Koyukuk region based on applying a simple classification threshold (that is, classifying all pixels with a reported permafrost probability below the threshold as not permafrost and all pixels with a reported permafrost probability above the threshold as permafrost). We sweep through all possible threshold values, from 0% to 100%, and compute the true positive and true negative rates, as well as the total accuracy. **e**, The threshold value of 40% yields the highest total classification accuracy. The true-negative, false-negative, false-positive and true-positive values for this classification are shown in the confusion matrix in **e**. The satellite imagery in **b** is from Bing Maps Aerial, reprinted with permission from Microsoft Corporation.

Extended Data Table 1 | Physical constants and parameters used for equations (3)–(6)

Variable	Description	Value	Units	Source
PHYSICAL CONSTANTS AND LITERATURE VALUES				
ρ_b	Bulk density of bank sediment	861	kg m^{-3}	Lininger et al. (2019)
f_{ice}	Mass fraction of ice in bank sediment	0.236	kg kg^{-1}	Lininger et al. (2019)
T_i	Initial bank temperature	-1	°C	Smith et al. (2022)
T_f	Fusion temperature for water ice	0	°C	
c_p	Heat capacity for bank sediment	3300	J kg^{-1} $°C^{-1}$	
L_{ice}	Latent heat of fusion for ice	3.34×10^5	J kg^{-1}	
α	Exponent on Pr in thaw model	0.333	dimensionless	Lunardini et al. (1986)
β	Exponent on Re in thaw model	0.927	dimensionless	Lunardini et al. (1986)
κ_w	Thermal conductivity of water	0.6	W m^{-1} $°C^{-1}$	
ν	Kinematic viscosity of water	1.00×10^{-6}	m^2 s^{-1}	
Pr	Prandtl number	10	dimensionless	Costard et al. (2003)
g	Gravitational acceleration	9.81	m s^{-2}	
ρ_w	Density of water	1000	kg m^{-3}	
n	Exponent in entrainment equation	1	dimensionless	Partheniades (1965)
M	Coefficient in entrainment equation	2.5×10^{-5}	kg m^{-2} s^{-1}	Partheniades (1965)
τ_{crit}	Critical shear stress required to entrain bank sediment	10^0–10^2	Pa	Dunne et al. (2020)
C_f	Friction coefficient for flow-resistance equation (eqn. 9)	5×10^{-3}	dimensionless	Phillips et al. (2022)
VALUES OPTIMIZED TO MATCH THE OBSERVED ANNUAL-AVERAGED EROSION RATES				
A [thaw]	Coefficient in thaw equation	3.2×10^{-22}	dimensionless	This study
M [entrainment]	Coefficient in entrainment equation	1.1×10^{-4}	kg m^{-2} s^{-1}	This study
τ_{crit} [entrainment]	Critical shear stress required to entrain bank sediment	3.5	Pa	This study
A [combined]	Coefficient in thaw equation	3.6×10^{-22}	dimensionless	This study
M [combined]	Coefficient in entrainment equation	7.5×10^{-3}	kg m^{-2} s^{-1}	This study
τ_{crit} [combined]	Critical shear stress required to entrain bank sediment	4.0	Pa	This study

Note that the parameters *A*, *M* and τ_{crit} are poorly constrained from the existing literature. In Extended Data Fig. 4i–k, we perform an optimization, allowing *A*, *M* and τ_{crit} to adopt the values such that the estimated annual erosion over the period 2017–2021 best matches the observations for the Koyukuk River (Extended Data Fig. 4l). The thaw-limited model has the free parameter {*A*}, the entrainment-limited model has the free parameters {*M*, τ_{crit}} and the combined model has all three free parameters {*A*, *M* and τ_{crit}}. Note that the improvement in the goodness of fit (quantified through R^2) from Extended Data Fig. 4i to Extended Data Fig. 4k could simply represent the increase in the number of tunable parameters from one (thaw-only) to two (entrainment-only) to three (combined thaw and entrainment). To try to address this effect arising from the change in the number of model parameters, we also compute the adjusted R^2 value (see equation (15)), which includes a penalty for models with more parameters. Sources: refs. 9,15,27,37,38,74,75.